PHYSICAL REVIEW E **104**, 065105 (2021)

Magnetic-field- and thermal-radiation-induced entropy generation in a multiphase nonisothermal plane Poiseuille flow

Joydip Chaudhuri [*]

Department of Chemical Engineering, Indian Institute of Technology Guwahati, Assam 781039, India

(Received 17 May 2021; accepted 23 November 2021; published 8 December 2021)

The effect of radiative heat transfer on the entropy generation in a two-phase nonisothermal fluid flow between two infinite horizontal parallel plates under the influence of a constant pressure gradient and transverse noninvasive magnetic field have been explored. Both fluids are considered to be viscous, incompressible, immiscible, Newtonian, and electrically conducting. The governing equations in Cartesian coordinates are solved analytically with appropriate boundary conditions to obtain the velocity and temperature profile inside the channel. Application of a transverse magnetic field is found to reduce the throughput and the temperature distribution of the fluids in a pressure-driven flow. The temperature and fluid flow inside the channel can also be noninvasively altered by tuning the magnetic field intensity, temperature difference between the channel walls and the fluids, and several intrinsic fluid properties. The entropy generation due to the heat transfer, magnetic field, and fluid flow irreversibilities can be controlled by altering the Hartmann number, radiation parameter, Brinkmann number, filling ratio, and ratios of fluid viscosities and thermal and electrical conductivities. The surfaces of the channel wall are found to act as a strong source of entropy generation and heat transfer irreversibility. The rate of heat transfer at the channel walls can also be tweaked by the magnetic field intensity, temperature differences, and fluid properties. The proposed strategies in the present study can be of significance in the design and development of next-generation microscale reactors, micro-heat exchangers, and energy-harvesting devices.

DOI: 10.1103/PhysRevE.104.065105

I. INTRODUCTION

Over the past few decades, scientific research related to micro- or nanoscale transport phenomena has shown a pathway to miniaturization with the rapid development of microfluidic devices such as microelectromechanical systems (MEMSs) [1,2], drug delivery systems [3], chemical separation devices [4], polymerase chain reactors [5–7], cell sorting devices [8,9], microreactors [10,11], micromixers [12], energy-harvesting devices [13,14], microscale biochemical analyzers [15], μ-total analysis systems [16,17], and biomedical instruments [18] to name a few. In these microfluidic flow systems, the dimensionless Reynolds number (Re) is almost always of a very small value, which defines that the flow in such systems is always laminar in nature [19,20]. A small value of Re is indicative of dominant viscous forces present in these flow systems. Due to these stronger viscous forces present, the laminar flow inside it can be effectively be classified as a plane Poiseuille flow if the channel walls are considered to be nonslipping and of negligible wall roughness [21]. However, due to the severe confinement and reduced length scales in such microfluidic devices, some unfavorable attributes have appeared in these flow systems which are driven by pressure actuation [22–26] in general, such as friction-induced power losses, biological sample dispersion, lack of precise control, and high flow-rate requirement.

In view of the aforementioned detrimental attributes, a noninvasive handle in the form of an externally applied field can add more flexibility to actuate such pressure-driven flows inside such microdomains. Recently, externally applied electric [27–30], magnetic [2,31–33], photonic [34–36], or acoustic [37,38] fields have been employed to disrupt the regular pressure-driven flows to improve the transport properties in such small length scales. Such external triggers help in effectively control of the balance between capillary, viscous, and inertial forces in order to augment the separation of flow features [9], improve surface-to-volume ratio [39], increase throughput [40], and enable mixing [12]. Among these external field-driven systems, magnetohydrodynamic (MHD) and electromagnetohydrodynamic (EMHD) micropumps and devices in general, driven by Lorentz force, have engrossed the scientific community due to certain advantages such as (1) absence of any mechanical moving parts, (2) *in situ* flow reversibility, and (3) higher throughput [41–44].

Design and fabrication of such a device requires an energy optimization that should address the various dissipative processes existing in such microflows which directly or indirectly affect their performance and efficacy. In fact, the nonintrusive application of electromagnetic fields in these devices introduces an additional energy dissipation that, along with fluid friction and heat transfer irreversibilities, must be measured carefully in order to provide the necessary power input to perform a certain task. However, miniaturization of these microfluidic devices demands an optimal power input to perform the desired tasks in order to achieve better overall efficiency and performance compared to the macrocounterpart. In order to reduce the overall energy utilization, some efficient microfluidic systems have been designed to reduce the amount

---

[*] joydipchaudhuri1@gmail.com

©2021 American Physical Society

of useless energy recently. Due to the impacts of energy dissipation owing to heat transfer and fluid friction, these useless energies can initiate the irreversibility of a fluidic system. In this regard, the concept of entropy generation minimization has engrossed much attention in fluid-thermal engineering, and one can minimize the entropy generation by optimizing the design parameters of such systems.

In view of this background, the detailed analysis of entropy generation seems to be an appropriate tool to assess the inherent irreversibilities in such microflows and to regulate optimized operating conditions that ensures a minimum energy dissipation consistent with the other physical constraints required by the system. Bejan introduced the analysis of entropy generation [45,46], which has been employed to assess the performance of various engineering applications such as heat exchangers [47], two-phase flows [48], or fuel cells [49], among many others. It has also been applied to ensure the optimization of energy input and output in the case of MHD flows in MHD pumps, electric generators [50–53], and fusion reactors [54]. The prior art suggests that the analysis of entropy generation in microchannels considering mainly the effects of viscous and thermal irreversibilities [55,56] is capable of uncovering the detailed physics associated with such microflows.

EMHD-induced heat transfer and the associated entropy generation play a major role in the field of heat and momentum transfer owing to multifarious applications in the liquid metal flows in the metallurgical industry [57], micropumps [33] and in the chemical [10,11], biomedical [3], and biological [8,9] sectors. Previous studies have also attempted to decipher the temperature distribution and heat transfer characteristics of EMHD flows, where the heat generation was due to the inherent Joule heating [58] or the electrokinetic effects associated with such flows [59]. However, these studies have ignored the coupling of the interactions between electric and magnetic fields in the energy equation. Jian *et al.* introduced these coupling terms in the energy equation to investigate the transient EMHD heat transfer and entropy generation in a parallel plate microchannel [60]. Recently, the study of entropy generation in a bilayer electroosmotic flow uncovered the velocity and temperature distribution and analytically evaluated the rate of entropy generation [60]. Apart from these, the entropy generation in EMHD flows and thermal transport characteristics of non-Newtonian fluids [61,62] and nanofluids [63] have fascinated numerous researchers in the recent past.

The literature reviewed above discusses the entropy generation analysis for a multitude of external field-induced fluid flows in a narrow conduit. However, all of these past works involve a single-phase fluid flow between two infinitely long but narrow width plates. Also, the literature discussed does not necessarily consider these type of bilayer EMHD flow under the influence of both a magnetic field and radiative heat transfer. The literature also does not provide a detailed parametric analysis of the heat transfer through temperature variations and the rate of heat transfer through the walls, describing the functioning of a potential micropump under scenarios analogous to the applications involving thermal management. The literature discussed so far suggests that a detailed analysis of the entropy generation in a multiphase nonisothermal plane Poiseuille bilayer fluid flow due to the combined effect of a transverse magnetic field and thermal radiation is yet to make an appearance. More specifically, in order to utilize the potential of relatively new technologies of EMHD devices, it is of vital importance to study the associated thermal characteristics within a more generic framework consisting of a bilayer flow and by considering all the essential aspects of the microscale physics.

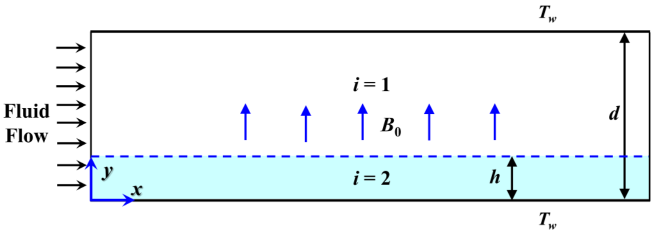

FIG. 1. Schematic diagram of a bilayer x-directional fluid flow under the combined influence of a transverse uniform magnetic field and radiative heat transfer from the parallel plates (not to scale). The distance between the parallel plates is d, and the thickness of the lower layer of fluid ($i = 2$, cyan region) is h. The temperatures of both parallel plates are constant and denoted by T_w. The strength of the uniform magnetic field is B_0.

Herein we analytically explore the characteristics of the entropy generation in a two-phase, bilayer, nonisothermal plane Poiseuille flow under the influence of a noninvasively applied transverse magnetic field and considering the effect of radiative heat transfer. The schematic diagram in Fig. 1 shows the typical geometry chosen for the analytical model. Employing a fully developed, steady, laminar Poiseuille flow model on a pair of electrically conducting, incompressible, nonisothermal, and immiscible fluids under the influence of a magnetic field and radiative heat transfer, an exact solution of governing equations for both fluid regions has been obtained in closed form. Contributions to the total entropy generation in the system due to heat transfer, magnetic field, and radiation are also evaluated analytically. The velocity and temperature distribution inside the channel and entropy generation are found to be dependent on various fluid properties such as viscosity and thermal and electrical conductivities, as well as on a number of external field parameters, namely, magnetic field intensity and conductive and radiative heat transfer parameters. A detailed parametric study has been carried out to see the effect of these pertinent parameters on the flow field, temperature field, and the entropy generation characteristics. We have also uncovered the contribution of heat transfer, magnetic field, and fluid flow irreversibilities to the total entropy generation for such a system, which provides an idea of the input energy budget for such a flow.

The remainder of the paper is organized in the following manner. In Sec. II the details of the theory and the problem formulation are discussed. It also contains the details of the dimensional and nondimensional governing equations, boundary conditions, and expressions for the distribution of velocity, temperature, and entropy generation. The results are discussed in detail in Sec. III, before conclusions are drawn in Sec. IV.

II. THEORETICAL FORMULATION

A. Problem formulation

We consider fully developed, steady, laminar Poiseuille flow of a pair of electrically conducting, incompressible, and immiscible fluids ($i = 1$ and 2) in a channel bounded by two plates under the effect of a transverse magnetic field B_0, which is applied normal to the flow direction. Both parallel plates are impermeable and maintained at a uniform temperature T_w. The x-axis is considered to be in the direction of fluid flow along the length of the channel, whereas the y-axis is taken normal to the lower plate along the width of the channel. The parallel plates are considered to be infinitely long, and the distance between them is d. The thickness of the lower layer of fluid ($i = 2$) is h. A representative schematic diagram of the problem under consideration is shown in Fig. 1. For the ith fluid, the notations $\mathbf{u}_i(u_i, v_i)$, t_i, ρ_i, η_i, σ_i, and k_i denote the velocity vector (velocity components), temperature, density, viscosity, electrical conductivity, and thermal conductivity, respectively. The magnetic Reynolds number is assumed to be small, so that the induced magnetic field can be neglected and the Hall effect of MHD is assumed to be negligible.

B. Dimensional governing equations and boundary conditions

The dynamics of the steady-state fully developed laminar Poiseuille flow of both fluids ($i = 1$ and 2) in a channel is governed by the equations of motions and continuity equation, which can be expressed as

$$-\nabla p_i + \nabla \cdot \left[\eta_i\left(\nabla \mathbf{u}_i + \nabla \mathbf{u}_i^T\right)\right] + \mathbf{F}_M = 0, \tag{1}$$

$$\nabla \cdot \mathbf{u}_i = 0. \tag{2}$$

The additional body force $\mathbf{F}_M$ in Eq. (1), also termed Lorentz force, is added due to the imposed uniform magnetic field $\mathbf{B}_0$ along the y-direction. Also, it is assumed that the associated electric field due to the application of uniform magnetic field is zero, i.e., $\mathbf{E}_0 = \nabla V = 0$. Therefore, from Ohm's law, we can express the current density J as $\mathrm{J}_i = \sigma_i(-\nabla V_i + \mathbf{u}_i \times \mathbf{B}_0) = \sigma_i(\mathbf{u}_i \times \mathbf{B}_0)$. The Lorentz force $\mathbf{F}_M$ in Eq. (1) then can be evaluated as $\mathbf{F}_M = \mathrm{J}_i \times \mathbf{B}_0 = \sigma_i(\mathbf{u}_i \times \mathbf{B}_0) \times \mathbf{B}_0 = -\sigma_i u_i B_0^2 \hat{\mathbf{x}}$, where $\hat{\mathbf{x}}$ is the unit vector along the x-direction. Since the fluid flow in the channel is considered to be only x-directional, therefore, applying the assumptions, the dimensional governing equations for both the fluids can be expressed as follows.

For $i = 1$, ($h \leqslant y \leqslant d$), the x-momentum balance equation can be written as

$$\eta_1 \frac{d^2 u_1}{dy^2} - \sigma_1 u_1 B_0^2 = \frac{dp}{dx}, \tag{3}$$

the y-momentum balance equation can be written as

$$\frac{dp}{dy} = 0, \tag{4}$$

the continuity equation can be expressed as

$$\frac{du_1}{dx} = 0, \tag{5}$$

and the energy balance equation can be expressed as

$$k_1 \frac{d^2 t_1}{dy^2} + \eta_1 \left(\frac{du_1}{dy}\right)^2 + \sigma_1 u_1^2 B_0^2 - \frac{dq_1^r}{dy} = 0. \tag{6}$$

For $i = 2$, ($0 \leqslant y \leqslant h$), the x-momentum balance equation can be written as

$$\eta_2 \frac{d^2 u_2}{dy^2} - \sigma_2 u_2 B_0^2 = \frac{dp}{dx}, \tag{7}$$

the y-momentum balance equation can be written as

$$\frac{dp}{dy} = 0, \tag{8}$$

the continuity equation can be expressed as

$$\frac{du_2}{dx} = 0, \tag{9}$$

and the energy balance equation can be expressed as

$$k_2 \frac{d^2 t_2}{dy^2} + \eta_2 \left(\frac{du_2}{dy}\right)^2 + \sigma_2 u_2^2 B_0^2 - \frac{dq_2^r}{dy} = 0. \tag{10}$$

The y-momentum balance and the continuity equation for both the fluids essentially signify that $p \neq f(y)$ and $u_i \neq f(x)$.

The dimensional boundary conditions can be stated as

$$\text{at} \quad y = 0, \quad u_2 = 0, \quad t_2 = T_w, \tag{11}$$

$$\text{at} \quad y = h, \quad u_1 = u_2, \quad \eta_2\left(\frac{du_2}{dy}\right) = \eta_1\left(\frac{du_1}{dy}\right), \tag{12}$$

$$\text{at} \quad y = h, \quad t_1 = t_2, \quad k_2\left(\frac{dt_2}{dy}\right) = k_1\left(\frac{dt_1}{dy}\right), \tag{13}$$

$$\text{and at} \quad y = d, \quad u_1 = 0, \quad t_1 = T_w. \tag{14}$$

Here B_0 is the magnetic field intensity, dq_i^r is the radiative heat flux, and $\frac{dp}{dx}$ is the applied pressure gradient. Furthermore, we neglected the effect of interface curvature at the fluid-fluid boundary in order to neglect the effect of interfacial tension and the additional Maxwell stresses along the interface [64]. The no-slip boundary conditions for the fluid flow near the wall mentioned in Eqs. (11) and (14) of the mathematical formulation are consistent with the typical microchannel flows or ultrathin film flows [28,30,33,39,65,66].

Following the equilibrium model of Cogley *et al.* [67], the expression for the radiative heat flux (dq_i^r) in Eqs. (6) and (10) can be expressed as

$$\frac{dq_i^r}{dy} = 4(t_i - T_w) \int_0^\infty K_{\lambda w}\left(\frac{\partial e_{b\lambda}}{\partial T}\right)_w d\lambda = 4I^*(t_i - T_w), \tag{15}$$

where $I^* = \int_0^\infty K_{\lambda w}(\frac{\partial e_{b\lambda}}{\partial T})_w d\lambda$, $K_{\lambda w}$ is the absorption coefficient at the plate and $e_{b\lambda}$ is Planck's constant.

C. Nondimensional governing equations and boundary conditions

The equations are reduced to dimensionless forms using the following scheme:

$$\left.\begin{aligned}
&\bar{u}_1=\frac{u_1}{u_0},\ \ \bar{u}_2=\frac{u_2}{u_0},\ \ \bar{y}=\frac{y}{d},\ \ a=\frac{h}{d},\ \ \bar{\eta}=\frac{\eta_2}{\eta_1},\ \ \bar{k}=\frac{k_2}{k_1},\\
&\bar{\sigma}=\frac{\sigma_2}{\sigma_1},\ \ \theta_1=\frac{t_1-T_w}{T_w},\ \ \theta_2=\frac{t_2-T_w}{T_w},\ \ \mathrm{Ha}_1^2=\frac{\sigma_1 B_0^2 d^2}{\eta_1},\\
&\mathrm{Br}_1=\frac{\eta_1 u_0^2}{k_1 T_w},\ \ \mathrm{Ha}_2^2=\frac{\sigma_2 B_0^2 d^2}{\eta_2}=\mathrm{Ha}_1^2\left(\frac{\bar{\sigma}}{\bar{\eta}}\right),\\
&\mathrm{Br}_2=\frac{\eta_2 u_0^2}{k_2 T_w}=\mathrm{Br}_1\left(\frac{\bar{\eta}}{\bar{k}}\right),\ \ F_1=\frac{4I^*d^2}{k_1},\ \text{ and}\\
&F_2=\frac{4I^*d^2}{k_2}=F_1\left(\frac{1}{\bar{k}}\right).
\end{aligned}\right\} \tag{16}$$

Here $u_0=-\frac{d^2}{\eta_1}\frac{dp}{dx}$ is the reference velocity, a is the filling ratio, $\bar{\eta}$ is the viscosity ratio, $\bar{k}$ is the thermal conductivity ratio, $\bar{\sigma}$ is the electrical conductivity ratio, Ha_i $(i=1,2)$ are the Hartmann numbers, Br_i $(i=1,2)$ are the Brinkman numbers, and F_i $(i=1,2)$ are the radiation parameters. The Hartman numbers Ha_i indicate the strength of the Lorentz forces compared to the viscous forces; the Brinkman numbers Br_i signify the ratio between heat produced by viscous dissipation and heat transported by molecular conduction; and the radiation parameters F_i measure the relative dominance of radiative to conductive heat transfer within the system.

Employing the nondimensional parameters, the dimensionless governing equations for fluid flow and temperature distribution can be expressed as follows.

For $i=1$, $(a\leqslant\bar{y}\leqslant 1)$, the x-momentum balance equation can be written as

$$\frac{d^2\bar{u}_1}{d\bar{y}^2}-\mathrm{Ha}_1^2\bar{u}_1+1=0, \tag{17}$$

and the energy balance equation can be expressed as

$$\frac{d^2\theta_1}{d\bar{y}^2}+\mathrm{Br}_1\left(\frac{d\bar{u}_1}{d\bar{y}}\right)^2+\mathrm{Ha}_1^2\mathrm{Br}_1\bar{u}_1^2-F_1\theta_1=0. \tag{18}$$

For $i=2$, $(0\leqslant\bar{y}\leqslant a)$, the x-momentum balance equation can be written as

$$\frac{d^2\bar{u}_2}{d\bar{y}^2}-\frac{\mathrm{Ha}_1^2}{\bar{\eta}}\bar{u}_2+\frac{1}{\bar{\eta}}=0, \tag{19}$$

and the energy balance equation can be expressed as

$$\frac{d^2\theta_2}{d\bar{y}^2}+\mathrm{Br}_2\left(\frac{d\bar{u}_2}{d\bar{y}}\right)^2+\mathrm{Ha}_2^2\mathrm{Br}_2\bar{u}_2^2-F_2\theta_2=0. \tag{20}$$

The corresponding dimensionless boundary conditions can be expressed as

$$\text{at}\quad \bar{y}=0,\quad \bar{u}_2=0,\quad \theta_2=0, \tag{21}$$

$$\text{at}\quad \bar{y}=a,\quad \bar{u}_1=\bar{u}_2,\quad \bar{\eta}\left(\frac{d\bar{u}_2}{d\bar{y}}\right)=\left(\frac{d\bar{u}_1}{d\bar{y}}\right), \tag{22}$$

$$\text{at}\quad \bar{y}=a,\quad \theta_1=\theta_2,\quad \bar{k}\left(\frac{d\theta_2}{d\bar{y}}\right)=\left(\frac{d\theta_1}{d\bar{y}}\right), \tag{23}$$

$$\text{and}\quad\text{at}\quad \bar{y}=1,\quad \bar{u}_1=0,\quad \theta_1=0. \tag{24}$$

The mathematical description of the system is nondimensionalized in the present study so that the applicability of the model becomes independent of the length scale of the problem. This in particular allows the nondimensional mathematical model to be well poised to describe the momentum and heat transfer mechanisms and the associated entropy generation characteristics of a low Re microchannel flow in the case where the channel walls are nonslipping and of negligible roughness [21]. Therefore, in a sense, the dimensionless description of the plane Poiseuille flow presented in this study can also be employed to properly describe the physics of a typical microchannel flow if the wall properties remain the same [68].

D. Expressions for velocity and temperature distribution

The nondimensional governing equations (17)–(20) are solved employing the corresponding boundary conditions (21)–(24), and after dropping the overbars for convenience, the solved expressions for velocity (u_i) profiles can be given by

$$u_1=A_1\cosh(\mathrm{Ha}_1 y)+A_2\sinh(\mathrm{Ha}_1 y)+\frac{1}{\mathrm{Ha}_1^2}, \tag{25}$$

$$u_2=A_3\cosh(My)+A_4\sinh(My)+\frac{1}{\eta M^2}. \tag{26}$$

The coefficients in Eqs. (25) and (26) are given by

$$\left.\begin{aligned}
&\mathrm{Ha}_1^2=\eta M^2, A_1=-\frac{A_2\mathrm{Ha}_1^2\sinh(\mathrm{Ha}_1)+1}{\mathrm{Ha}_1^2\cosh(\mathrm{Ha}_1)},\\
&A_2=\frac{(1/\mathrm{Ha}_1)\alpha+(1/M)\beta}{\eta M\gamma+\mathrm{Ha}_1\delta}, A_3=-\frac{1}{\eta M^2},\\
&A_4=\frac{A_1\lambda+A_2\phi+\left(1/\mathrm{Ha}_1^2\right)+A_3(1-\psi)}{\omega},\\
&\alpha=\omega\phi, \beta=\cosh(\mathrm{Ha}_1)-\lambda\psi,\\
&\gamma=\psi\sinh[\mathrm{Ha}_1(1-a)],\\
&\delta=\omega\cosh[\mathrm{Ha}_1(1-a)],\\
&\lambda=\cosh(\mathrm{Ha}_1 a), \phi=\sinh(\mathrm{Ha}_1 a),\\
&\psi=\cosh(\mathrm{Ma})\quad\text{and}\quad\omega=\sinh(\mathrm{Ma}).
\end{aligned}\right\} \tag{27}$$

The solved expressions for the temperature θ_i profiles can be expressed as

$$\theta_1=P(\cosh R-\sinh R), \tag{28}$$

$$\theta_2=Q(\cosh S-\sinh S), \tag{29}$$

where $R=2y(\sqrt{F_1}+\mathrm{Ha}_1)$ and $S=2y(\sqrt{F_2}+M)$.

The complex expressions of the coefficients P and Q in Eqs. (28) and (29) are calculated using Mathematica. The mathematical expressions of these coefficients are given in Appendix A.

E. Entropy generation

The thermodynamic irreversibility within the system considered can be characterized by the existence of entropy in the system. Therefore, the calculation of entropy generation can be a convenient tool to quantitatively measure of irreversibility associated with the process. The local volumetric rate of entropy generation $[(S''')_i\ , \forall i=1,2]$ in the presence of a magnetic field for both fluids can be calculated as follows [69,70]:

For $i = 1$ ($h \leqslant y \leqslant d$),

$$(S''')_1 = \frac{k_1}{T_w}\left(\frac{dt_1}{dy}\right)^2 + \frac{1}{T_w}\left[\eta_1\left(\frac{du_1}{dy}\right)^2 + \sigma_1 B_0^2 u_1^2\right], \quad (30)$$

and for $i = 2$ ($0 \leqslant y \leqslant h$),

$$(S''')_2 = \frac{k_2}{T_w}\left(\frac{dt_2}{dy}\right)^2 + \frac{1}{T_w}\left[\eta_2\left(\frac{du_2}{dy}\right)^2 + \sigma_2 B_0^2 u_2^2\right]. \quad (31)$$

The nondimensional form of the entropy generation number (S_i^N) in both regions can be expressed as, for $i = 1$ ($a \leqslant y \leqslant 1$),

$$S_1^N = \frac{(S''')_1}{(S''')_0} = \left(\frac{d\theta_1}{dy}\right)^2 + \mathrm{Br}_1\left[\left(\frac{du_1}{dy}\right)^2 + \mathrm{Ha}_1^2 u_1^2\right], \quad (32)$$

and for $i = 2$ ($0 \leqslant y \leqslant a$),

$$S_2^N = \frac{(S''')_2}{(S''')_0} = k\left(\frac{d\theta_2}{dy}\right)^2 + k\mathrm{Br}_2\left[\left(\frac{du_2}{dy}\right)^2 + \mathrm{Ha}_2^2 u_2^2\right]. \quad (33)$$

In expressions (32) and (33), $(S''')_0 = \frac{k_1}{d^2}$ is the reference volumetric entropy generation, the heat transfer irreversibility (HTI) in the fluid 1 ($i = 1$) is $\mathrm{HTI}_1 = (\frac{d\theta_1}{dy})^2$, the fluid friction irreversibility (FFI) in the fluid 1 ($i = 1$) is $\mathrm{FFI}_1 = \mathrm{Br}_1(\frac{du_1}{dy})^2$, the magnetic field irreversibility (MFI) in the fluid 1 ($i = 1$) is $\mathrm{MFI}_1 = \mathrm{Br}_1\mathrm{Ha}_1^2 u_1^2$, the heat transfer irreversibility (HTI) in the fluid 2 ($i = 2$) is $\mathrm{HTI}_2 = k(\frac{d\theta_2}{dy})^2$, the fluid friction irreversibility in the fluid 2 ($i = 2$) is $\mathrm{FFI}_2 = k\mathrm{Br}_2(\frac{du_2}{dy})^2$, and the magnetic field irreversibility in the fluid 2 ($i = 2$) is $\mathrm{MFI}_2 = k\mathrm{Br}_2\mathrm{Ha}_2^2 u_2^2$. These irreversibilities can be evaluated by using the following dimensionless numbers, termed Bejan numbers ($\mathrm{Be}_i, i = 1, 2$), magnetic field irreversibility parameters ($\mathrm{I}_i, i = 1, 2$), and fluid flow irreversibility parameters ($\mathrm{J}_i, i = 1, 2$). The mathematical expressions of these dimensionless numbers (Be_i, I_i, and J_i, $i = 1, 2$) can be given by

$$\mathrm{Be}_i = \frac{\mathrm{HTI}_i}{S_i^N} = \frac{(d\theta_i/dy)^2}{(d\theta_i/dy)^2 + \mathrm{Br}_i\left[(du_i/dy)^2 + \mathrm{Ha}_i^2 u_i^2\right]}, \quad (34)$$

$$\mathrm{I}_i = \frac{\mathrm{MFI}_i}{S_i^N} = \frac{\mathrm{Ha}_i^2\mathrm{Br}_i u_i^2}{(d\theta_i/dy)^2 + \mathrm{Br}_i\left[(du_i/dy)^2 + \mathrm{Ha}_i^2 u_i^2\right]}, \quad (35)$$

$$\mathrm{J}_i = \frac{\mathrm{FFI}_i}{S_i^N} = \frac{\mathrm{Br}_i(du_i/dy)^2}{(d\theta_i/dy)^2 + \mathrm{Br}_i\left[(du_i/dy)^2 + \mathrm{Ha}_i^2 u_i^2\right]}. \quad (36)$$

III. RESULTS AND DISCUSSION

The study of fully developed, steady, laminar Poiseuille flow of a pair of electrically conducting, incompressible fluids (i =1 and 2) in a channel bounded by two plates under the effect of a transverse magnetic field and nonisothermal temperature field can be entirely characterized by six fundamental physical properties, namely, the viscosities, thermal, and electrical conductivities. Since we are considering the fluid flow to be in a Stokes flow regime, the effect of the fluid densities ρ_i is negligible. Apart from these, the dynamics of the problem depends on the filling ratio a, applied magnetic field intensity B_0, and temperature differences θ_i of both the fluids and the channel walls. Since all ten parameters involve three fundamental units (mass, time, and length), the problem can be characterized with seven independent dimensionless parameters. We can select these independent dimensionless parameters as a, η, k, σ, Ha_1, Br_1, and F_1. The physical significance of these dimensionless quantities was described in Sec. II C.

It may be noted here that the dimensionless numbers Ha_2, Br_2, and F_2 for fluid 2 can be expressed in terms of Ha_1, Br_1, and F_1 as shown in Eq. (16). To understand the effect of these seven dimensionless parameters on the fluid flow or the velocity distribution, temperature distribution, and by extension the entropy generation within the channel, a systematic study has been carried out over a range of a, η, k, σ, Ha_1, Br_1, and F_1.

A. Effect of filling ratio *a*

Figures 2(a)–2(d) show the variation of velocity u along the width y of the channel with increasing filling ratios a. Figures 2(a)–2(d) show that with increase in a from 0.1 to 0.8, the maximum as well as the average velocity of the fluids inside the channel decreases. The viscosity ratio η in these cases is kept constant at 2. With the increase in a, the channel gets filled with the more viscous fluid 2, which ensures that fluid 2 as well as fluid 1 (because of the laminar nature of the flow) flows slowly inside the channel.

Figures 2(e)–2(h) show the variation of temperature θ along the width y of the channel with increasing filling ratios a. Figures 2(e)–2(g) show that with an increase in a from 0.1 to 0.6, the maximum as well as average temperature of the fluids inside the channel increases. The slowly flowing fluids due to the increase in filling ratio retains more heat with them, which in turn increases the temperature distribution inside the channel. However, with a further increase in filling ratio ($a =$ 0.8), the temperature of the fluids decreases considerably as shown in Fig. 2(h).

The expressions for u_i and θ_i [Eqs. (25)–(26) and (28)–(29)] show that the velocity u_i of the fluids inside the channel essentially depends on a, η, and Ha_1 only, whereas the temperature θ distribution depends on the combined effect of all the seven dimensionless parameters as well as the velocity u profile inside the channel. For low filling ratios ($a = 0.1$–0.6), the temperature distribution essentially depends on the velocity u profile of the fluids inside rather than the combined effect of the other dimensionless parameters such as k, σ, Br_1, and F_1. However, for higher filling ratios, such as in the case of $a = 0.8$ [Fig. 2(h)], the effect of these dimensionless parameters (k, σ, Br_1, and F_1) dictates the temperature distribution inside the channel rather than the velocity profile of the fluids alone. This is the reason behind the apparent decrease in maximum as well as average temperature inside the channel with the filling ratio, $a = 0.8$ in Fig. 2(h).

Figures 3(a)–3(d), 3(e)–3(h), and 3(i)–3(l) show the variation of Bejan number Be, magnetic field irreversibility parameter I, and fluid flow irreversibility parameter J across the width y of the channel for different filling ratios a, respectively. Figures 3(a)–3(d) show that with an increase in filling ratio a, Be across the channel width y increases. Figure 3(a) shows that, for $a = 0.1$, the contribution in the entropy

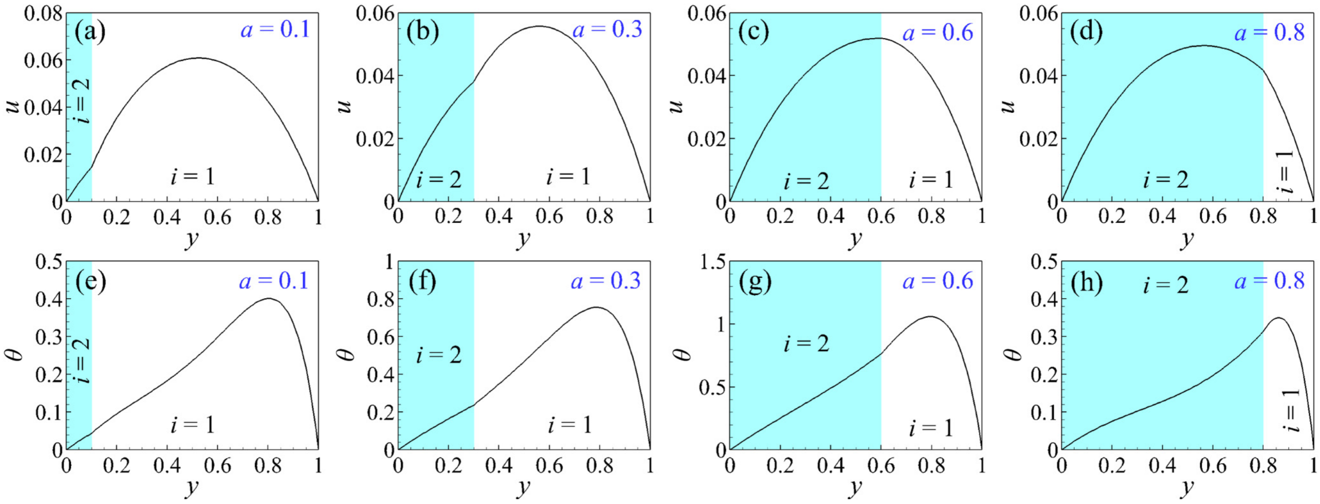

FIG. 2. Plots (a)–(d) and (e)–(h) show the velocity u and temperature θ distribution across the width y of the channel for different filling ratios a, respectively. The other parameters are $\eta = 2.0$, $\mathrm{Ha}_1 = 3.0$, $k = 1.5$, $\sigma = 1.0$, $\mathrm{Br}_1 = 2.0$, and $F_1 = 2.0$.

generation due to HTI or Be throughout the midsection of the channel ($0.1 \leqslant y \leqslant 0.9$) is negligible. With the increase in a, Be across the channel width y increases; however, there exists some minima across the width where the contribution in the entropy generation due to HTI is zero, such as for Fig. 3(b) $y \sim 0.1$, ~ 0.3, and ~ 0.8, for Fig. 3(c) $y \sim 0.5$, and for Fig. 3(d) $y \sim 0.6$.

Figures 3(e)–3(h) show that with an increase in filling ratio a, I, or the entropy generation due to MFI across the channel width y decreases as an average; however, $\mathrm{I}^{\max}$ ($\sim$0.8–1.0) remains similar. The locations of this maximum entropy generation due to MFI ($\mathrm{I}^{\max}$) are the same as the locations of the minima in the case of HTI in Figs. 3(a)–3(d), which signifies that the across the channel width y there are some zones where the entropy generation due to HTI (MFI) is highest (lowest) and vice versa.

Figures 3(i)–3(l) show that the entropy generation due to the FFI (or the dimensionless number J) decreases with the

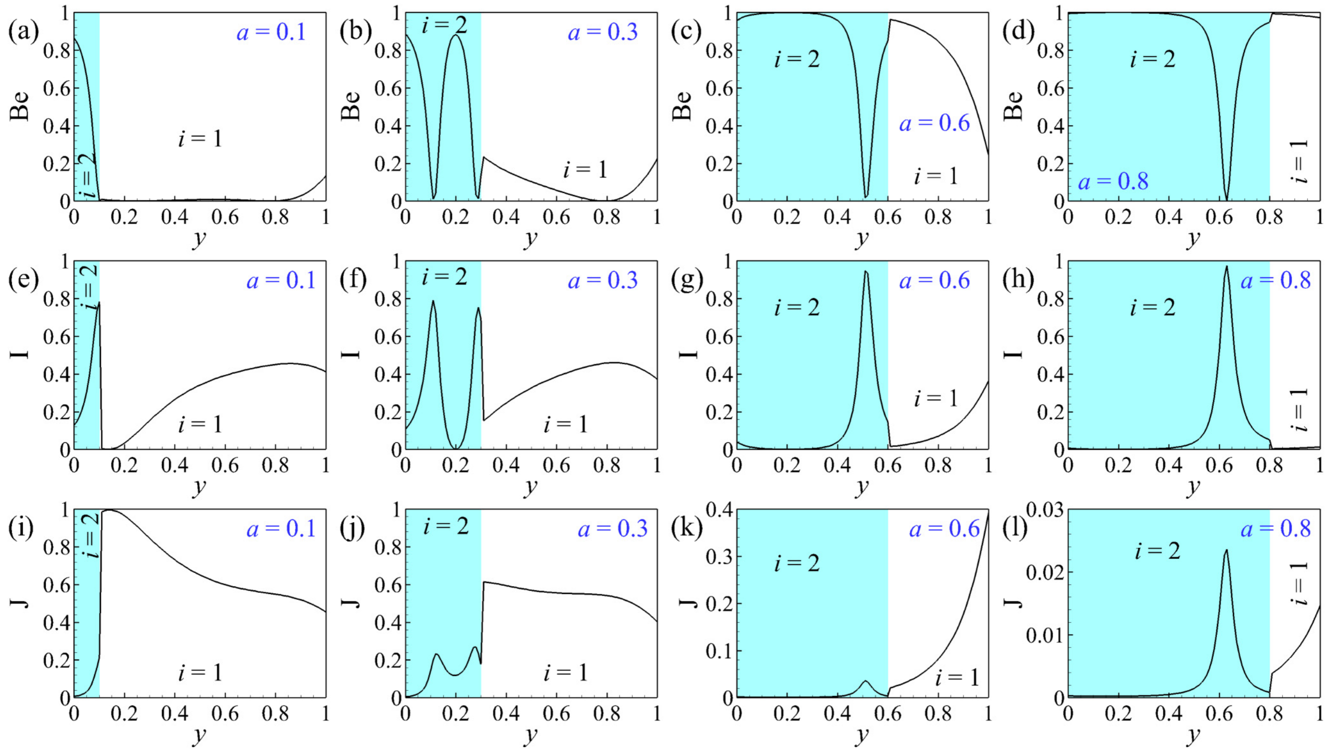

FIG. 3. Plots (a)–(d), (e)–(h), and (i)–(l) show the variation of Bejan number Be, magnetic field irreversibility parameter I, and fluid flow irreversibility parameter J across the width y of the channel for different filling ratios a, respectively. The other parameters are $\eta = 2.0$, $\mathrm{Ha}_1 = 3.0$, $k = 1.5$, $\sigma = 1.0$, $\mathrm{Br}_1 = 2.0$, and $F_1 = 2.0$.

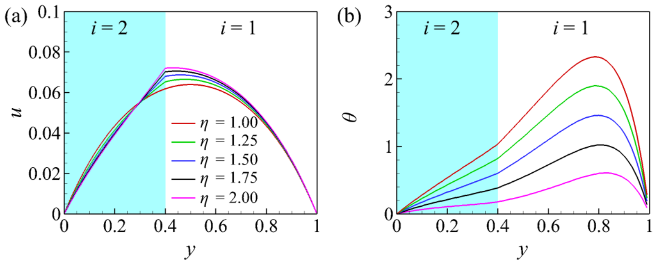

FIG. 4. Plots (a) and (b) show the variation of velocity u and temperature θ across the width y of the channel for different viscosity ratios η, respectively. The other parameters are $a = 0.4$, $\mathrm{Ha}_1 = 3.0$, $k = 1.5$, $\sigma = 1.0$, $\mathrm{Br}_1 = 5.0$, and $F_1 = 2.0$.

increase in filling ratio a across the width y of the channel because of the less fluid flow as shown in Figs. 2(a)–2(d). However, it is interesting to note that, when the filling ratio a is comparatively lower ($= 0.1$) in Fig. 3(i), the contribution in maximum entropy generation due to FFI (~ 1.0) near the interface is entirely due to the relatively unhindered fluid flow in the channel. Although with the increase in a, the contribution to entropy generation due to the FFI (or J) near the fluid-fluid interface decreases [~ 0.6 for $a = 0.3$ in Fig. 3(j) and ~ 0.0 for $a = 0.6$ and 0.8 in Figs. 3(k) and 3(l)] and is predominantly determined by the contribution from HTI (or Be).

B. Effect of viscosity ratio η

Figures 4(a) and 4(b) display the variation of velocity u and temperature θ along the width (y) of the channel with increasing viscosity ratios η, respectively. First, when $\eta = 1.0$, the red line in Fig. 4(a) shows that the velocity profile is parabolic and consistent with the plane Poiseuille flow. Figure 4(a) also shows that, initially up to $y \sim 0.3$, with the increase in η, the velocity of fluid 2 is decreasing. However, beyond that the velocity of the fluids increases with an increase in η. Increasing the ratio η also decreases the dimensionless number Ha_2 (as $\mathrm{Ha}_2 \propto 1/\sqrt{\eta}$), which augments the flow of fluid 2 inside the channel. In order to maintain the flow rate inside the channel due to the mass balance arising from the continuity equations [Eqs. (5) and (9)], the velocity of fluid 1 increases with the increase in η. At the fluid-fluid interface, the high velocity of fluid 1 essentially increases the velocity of fluid 2 due to the laminar nature of the flow.

With the increase in viscosity ratio η, the temperature of both fluids decreases as shown in Fig. 4(b). We have already discussed in Fig. 2 that, for low filling ratios ($a = 0.1$–0.6), the temperature distribution essentially depends on the velocity u profile of the fluids inside rather than the combined effect of the other heat-transfer-related dimensionless parameters. In the case of Fig. 4(b), since $a = 0.4$, the temperature profile of the fluids mainly depends on the velocity profile.

Figure 4(a) shows that the velocity of fluid 1 is increasing with the increase in η, whereas the velocity of fluid 2 is slightly decreasing, which is why the temperature of fluids 1 and 2 decreases with the increase in η. It is noteworthy that the velocity profile in Fig. 4(a) shows that the maximum velocity inside the channel is near the midline ($y = 0.4$–0.6), whereas the temperature profile shows that the maximum temperature is near $y = 0.8$, which is near the upper wall of the channel. The maximum temperature inside the channel is dictated by the heat transfer mechanisms, which are directly correlated to the combined effect of the dimensionless parameters, k, σ, Br_1, and F_1.

Figure 5(a) shows that, with the increase η, the contribution in the entropy generation due to HTI or Be increases across the channel width y. Since an increase in η from 1 to 2 reduces the flow of fluid 2 inside the channel, the entropy generation due to HTI in fluid 2 quadruples as shown in Fig. 5(a). However, the minima in Fig. 5(a) near $y = 0.8$ shows that the entropy generation due to HTI (or Be) at that location is negligible. It is noteworthy that this is the same location where the temperature inside the channel is maximum as shown in Fig. 4(b).

Figure 5(b) shows that, for a particular η, the entropy generation due to MFI (or I) initially decreases, goes through a minimum near $y = 0.2$, then increases, and goes through a maximum near $y = 0.8$. It is also interesting to note that I is always less than 0.5 throughout the channel width y for all the viscosity ratios η, which signifies that $\mathrm{Be} + \mathrm{J} > \mathrm{I}$ or $\mathrm{HTI} + \mathrm{FFI} > \mathrm{MFI}$. This also represents that changing the viscosity ratio essentially changes the velocity and the temperature profile inside the fluids, which in turn dictates the HTI and the FFI. However, the entropy generation due to the magnetic field (MFI) is not directly dependent on η; rather it depends mainly on the flow and temperature profile change inside the channel due to the change in η.

Figure 5(c) depicts that J decreases with the increase in η across the channel width (y). It can be seen from Fig. 5(c) that, when η is lower, the maximum contribution to entropy

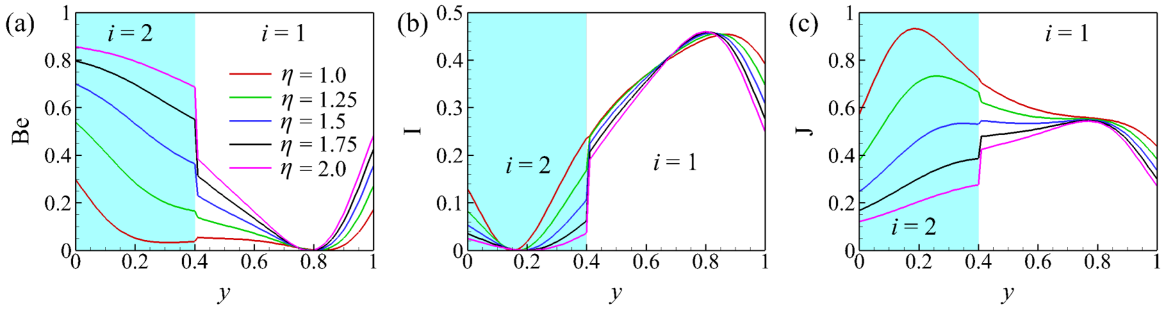

FIG. 5. Plots (a), (b), and (c) show the variation of Bejan number Be, magnetic field irreversibility parameter I, and fluid flow irreversibility parameter J across the width y of the channel for different viscosity ratios η, respectively. The other parameters are $a = 0.4$, $\mathrm{Ha}_1 = 3.0$, $k = 1.5$, $\sigma = 1.0$, $\mathrm{Br}_1 = 5.0$, and $F_1 = 2.0$.

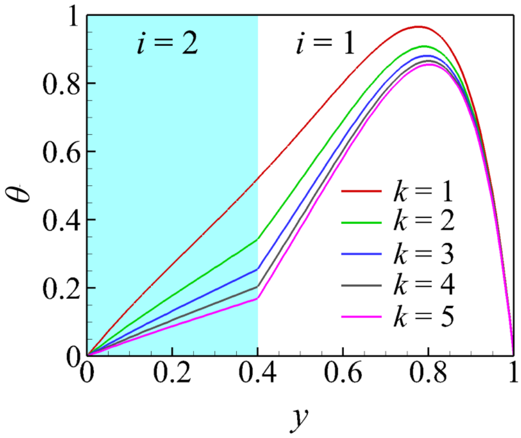

FIG. 6. The temperature θ distribution across the width y of the channel for different thermal conductivity ratios k, respectively. The other parameters are $a = 0.4$, $\mathrm{Ha}_1 = 3.0$, $\eta = 2.0$, $\sigma = 1.0$, $\mathrm{Br}_1 = 2.0$, and $F_1 = 2.0$.

generation inside fluid 2 is due to the FFI compared to HTI and MFI. This is because the lesser value of η enhances the fluid flow inside the channel, which in turn increases the entropy generation due to fluid flow. FFI goes through a maximum near $y = 0.2$ in Fig. 5(c) for $\eta = 1$ or 1.25. Figure 5(c) also shows a second local maxima near $y = 0.8$ (fluid 1), where $\mathrm{J} \sim 0.5$ or more, which is the same location where I also goes through a local maximum as shown in Fig. 5(b). This signifies that, in the fluid 1 region near $y = 0.8$, the entropy generation is mainly dictated by the combined effect from the magnetic field (MFI) and the fluid flow (FFI) rather than the heat transfer component (HTI).

Figure 5 shows that the entropy generation inside the channel can be varied by altering the ratio η and the mechanism of entropy generation for both fluids differ accordingly. The entropy generation due to FFI plays a major role for both fluids (contribution $\geqslant 50\%$); however, MFI (HTI) contributes less in the case of fluid 2 (fluid 1) in the overall entropy generation inside the channel with the increase in the viscosity ratio.

C. Effect of thermal conductivity ratio *k*

Figure 6 shows the temperature profile across the width y of the channel for different thermal conductivity ratios k. The heat transfer due to conduction inside the channel increases due to the increase in k, which decreases the temperature θ of the fluids as shown in Fig. 6. The thermal conductivity ratio k in our case is evaluated as the ratio of thermal conductivity of fluid 2 with fluid 1 ($k = k_2/k_1$). This ensures that at higher k, the temperature of fluid 2 (cyan region) decreases more rapidly than in fluid 1 (white region). Also, the maximum temperature of fluid 1 is more than fluid 2 because of the fluid flow conditions maintained by the flow parameters, $\eta = 2.0$, and $\mathrm{Ha}_1 = 3.0$. The maximum temperature of fluid 1 actually is near $y = 0.8$, which is near the upper wall of the channel and similar to Fig. 4(b) due to the similar flow and thermal parameters.

Figure 7(a) shows that, with the increase k, the contribution in the entropy generation due to HTI or Be decreases across the channel width y. Since an increase in k reduces the temperature distribution inside the channel, the entropy generation due to HTI in fluid 2 declines significantly as shown in Fig. 7(a). Although the value of Be for fluid 1 always remains lower ($\mathrm{Be}_1 \leqslant 0.3$) than that of fluid 2 ($\mathrm{Be}_2 \geqslant 0.3$), there is a stark contrast between the variation of Be_1 and Be_2. It can be interpreted from Fig. 7(a) that, other than the global minima near $y = 0.8$, Be_1 always increases with the increase in k, although Be_2 decreases with the increase in k. However, the minima in Fig. 7(a) near $y = 0.8$ shows that the entropy generation due to HTI (or Be) at that location is almost negligible. It is interesting to note that this is the same location where the temperature inside the channel is maximum as shown in Fig. 6.

Figure 7(b) shows that, for a particular k, the entropy generation due to MFI (or I) initially decreases, goes through a minimum near $y = 0.2$, then increases, and goes through a maximum near $y = 0.8$. It is important to note that I is always less than 0.5 throughout the channel width for all thermal conductivity ratios k, which signifies that $\mathrm{Be} + \mathrm{J} > \mathrm{I}$ or $\mathrm{HTI} + \mathrm{FFI} > \mathrm{MFI}$. This also represents that changing k essentially changes the temperature profile inside the fluids, which in turn dictates the HTI and the FFI. However, the entropy generation due to the magnetic field (MFI) is not directly dependent on k; rather it depends mainly on the flow and temperature profile change inside the channel due to the change in k. Furthermore, the entropy generation due to MFI (or I) near the fluid-fluid interface suddenly increases greater than $\sim 10\%$ from fluid 2 ($\mathrm{I}_2 < 0.1$) to fluid 1 ($\mathrm{I}_1 > 0.2$) irrespective of the value to k, which is also an important factor in considering the

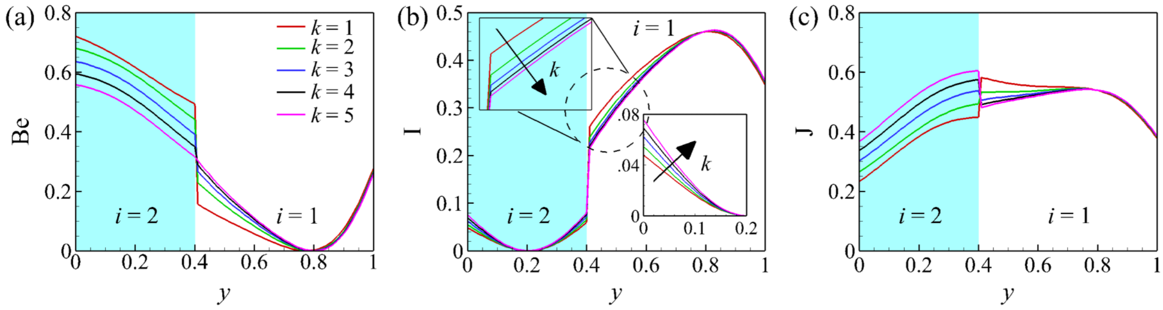

FIG. 7. Plots (a), (b), and (c) show the variation of Bejan number Be, magnetic field irreversibility parameter I, and fluid flow irreversibility parameter J across the width y of the channel for different thermal conductivity ratios k, respectively. The other parameters are $a = 0.4$, $\mathrm{Ha}_1 = 3.0$, $\eta = 2.0$, $\sigma = 1.0$, $\mathrm{Br}_1 = 2.0$, and $F_1 = 2.0$.

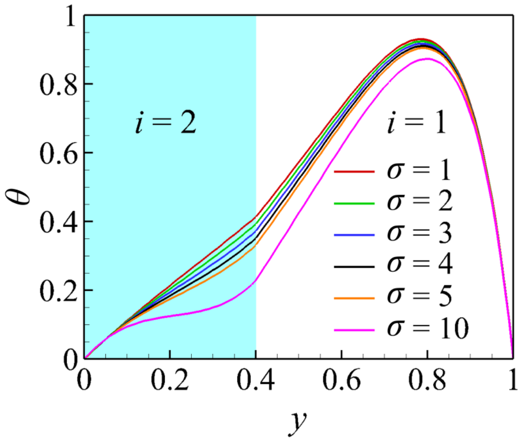

FIG. 8. The temperature θ distribution across the width y of the channel for different electrical conductivity ratios σ, respectively. The other parameters are $a = 0.4$, $\mathrm{Ha}_1 = 3.0$, $\eta = 2.0$, $k = 1.5$, $\mathrm{Br}_1 = 2.0$, and $F_1 = 2.0$.

irreversibility due to the presence of a fluid-fluid interface in Fig. 7(b). Figure 7(b) also shows that, other than the global minima (maxima) near $y = 0.2(0.8)$, $\mathrm{I}_1(\mathrm{I}_2)$ always decreases (increases) with the increase in k, as shown clearly in the inset of Fig. 7(b).

Figure 7(c) depicts that $\mathrm{J}_1(\mathrm{J}_2)$ always decreases (increases) with the increase in k, across the channel width. It can be seen from Fig. 7(c) that, when k is lower (1, for example), the maximum contribution to entropy generation inside fluid 2 is due to HTI (contribution ∼70%) compared to FFI (contribution ∼20%) and MFI (contribution ∼10%). This is because the lesser value of k enhances the temperatures of the fluids inside the channel, which in turn increases the entropy generation due to HTI. Figure 7(c) also shows that irrespective of the fluids, the contribution to the total entropy generation inside the channel due to FFI is always within 20%–60%. This signifies that even though the thermal conductivity ratio does not necessarily change the fluid flow inside the channel as such, a significant portion of the total entropy generation due to fluid flow can be controlled by controlling k.

In summary, Fig. 7 shows that, due to the change in k, the entropy generation inside the channel can be varied; also, the mechanism of entropy generation for both the fluids differs significantly. The entropy generation due to HTI plays a major role for fluid 2 (contribution $\geqslant$ 40%); however, in the case of fluid 1 the overall entropy generation mainly is dictated by FFI (contribution $\geqslant$ 40%).

D. Effect of electrical conductivity ratio σ

Figure 8 shows the temperature profile across the width y of the channel for different electrical conductivity ratios σ. Increasing the ratio σ increases the dimensionless number Ha_2 (as $\mathrm{Ha}_i \propto \sqrt{\sigma_i}$), which hinders the flow of fluid 2 inside the channel. When the velocity of fluid 2 decreases inside the channel, the heat transfer via radiative mode increases. Figure 8 shows that this low fluid velocity facilitates the considerable temperature drop (from $\theta_2^{avg} \sim 0.3$ to $\theta_2^{avg} \sim 0.1$, $\Delta\theta_2^{avg} \sim 0.2$) in fluid 2, whereas the drop in the fluid 1 temperature is considerably lower ($\Delta\theta_2^{avg} \leqslant 0.1$).

Figure 9(a) shows that, with the increase in σ, the contribution in the entropy generation due to HTI or Be decreases in fluid 2. Since an increase in σ reduces the temperature distribution inside the channel, the entropy generation due to HTI in fluid 2 declines significantly as shown in Fig. 9(a). Although the value of Be for fluid 1 (Be_1) always remains lower ($\leqslant 0.25$) than that of fluid 2 ($\mathrm{Be}_2 \geqslant 0.35$) for most of the cases ($\sigma \leqslant 5.0$), but there is a significant contrast between the variation of Be_1 and Be_2 with the variation in σ. It can be interpreted from Fig. 9(a) that, other than the global minima near $y = 0.8$, the variation of Be_1 always remains similar with the increase in σ, although Be_2 decreases with the increase in σ. The global minima in Fig. 9(a) near $y = 0.8$ shows that the entropy generation due to HTI (or Be) at that location is almost negligible. It is important to note that this is the same location where the temperature inside the channel is maximum as shown in Fig. 8.

Another interesting observation from Fig. 9(a) is that, in fluid 2, Be_2 initially decreases with the increase in y, and eventually increases with further increase in y. Also, with the increase in σ, the rate of decrease or increase (minimum Be_2, $\mathrm{Be}_2^{\min}$) of Be_2 in fluid 2 increases (decreases) as shown in Fig. 9(a). For example, $\mathrm{Be}_2^{\min} \sim 0.4$ at $y = 0.3$ for $\sigma = 4.0$ in fluid 2 gets shifted to $\mathrm{Be}_2^{\min} \sim 0.05$ at $y = 0.2$ for $\sigma = 10.0$.

Figure 9(b) shows that, for all σ (= 1–10), the entropy generation due to MFI in fluid 1 (or I_1) initially increases, goes through a maximum near $y = 0.8$, then decreases, although the magnitude of I_1 varies minimally across the width of the channel ($a \leqslant y \leqslant 1$) for increasing σ. However, increasing σ

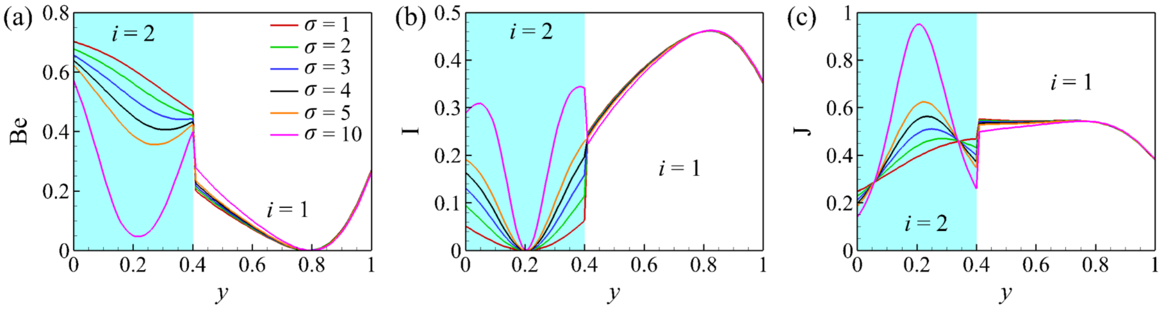

FIG. 9. Plots (a), (b), and (c) show the variation of Bejan number Be, magnetic field irreversibility parameter I, and fluid flow irreversibility parameter J across the width y of the channel for different electrical conductivity ratios σ, respectively. The other parameters are $a = 0.4$, $\mathrm{Ha}_1 = 3.0$, $\eta = 2.0$, $k = 1.5$, $\mathrm{Br}_1 = 2.0$, and $F_1 = 2.0$.

changes the distribution of I_2 across the width of the channel ($0 \leqslant y \leqslant a$) for fluid 2. For almost all σ ($=$ 1–5), I_2 initially decreases with increase in y, then goes through a minimum near $y = 0.2$, and then increases with further increase in y till $y \leqslant a$.

Figure 9(b) shows that, near the wall ($y = 0$) and the interface of fluids 1 and 2 ($y = a$), the magnitude of I_2 remains maximum, and this maximum magnitude increases with the increase in σ. This distribution implies that, with the increase in electrical conductivity of fluid 2, the entropy generation due to MFI increases near the wall and the interface. However, with further increase in $\sigma (= 10)$ the variation I_2 changes significantly across fluid 2 ($0 \leqslant y \leqslant a$). The variation of I_2 for $\sigma = 10$ in Fig. 9(b) shows that, near the lower wall ($y = 0$) and the fluid-fluid interface ($y = a$), the magnitude of I_2 briefly goes through a pair of local maximums at $y = 0.05$ and $y = 0.35$. This apparent shift of local maximums from the wall ($y = 0$) and the interface ($y = a$) towards the inner regions of fluid 2 ($y = 0.05$ and $y = 0.35$) implies that, with the increase in orders of magnitude of σ (1 to 10) the entropy generation due to MFI shifts towards the bulk of the fluid 2. It is also interesting to note that I is always less than 0.5 throughout the channel width for all σ ($=$ 1–10), which signifies that Be+J > I, or HTI+FFI > MFI.

Figure 9(c) illustrates that J_1 always remains similar with the increase in σ, although J_2 varies significantly with the increase in σ. It can be seen from Fig. 9(c) that, for $\sigma = 1$, J_2 increases monotonically with the increase in y up to $y \leqslant a$, whereas, for $\sigma = 2 - 10$, J_2 initially increases monotonically with the increase in y up to a certain value and then decreases with further increase in y up to $y \leqslant a$. This distribution ensures that near the wall ($y = 0$) and the fluid-fluid interface ($y = a$) the entropy generation due to FFI (or J_2) actually decreases with the increase in σ. Also, Fig. 9(c) shows that the maximum $J_2(J_2^{\max})$ shifts minutely from $y > a/2$ towards $y \sim a/2$ with the increase σ from 2 to 10.

In short, Fig. 9 shows that the magnitudes and mechanisms of entropy generation inside the channel can be altered by changing σ for both the fluids. For most of the cases, the entropy generation due to FFI and HTI plays a major role for fluid 2 (total contribution $\geqslant$70%); however, in the case of fluid 1 the overall entropy generation is mainly dictated by FFI and MFI (total contribution $\geqslant$70%).

E. Effect of Hartmann number Ha_1

Figures 10(a) and 10(b) show the variation of velocity u and temperature θ along the width y of the channel with increasing Hartmann numbers Ha_1, respectively. An increase in Ha_1 increases the effect of the Lorentz force inside the channel, which acts as a resistance to the flow. Therefore, it is observed that the velocity in the channel decreases with the increase in the value of Ha_1. Duwairi *et al.* showed in a previous study that for a single fluid under the influence of a transverse magnetic field, the magnitudes of velocity and temperature distribution decrease with the increase in Ha [58]. This means that the electrical conductivity of the fluid dictates the velocity and the temperature profiles. We have also modified the present mathematical formulation to asymptotically match the governing equations of Duwairi *et al.* by employing the same fluid properties for both fluids in order to mimic a single-fluid system [58]. The results from this asymptotic study show a good match with the results of Duwairi *et al.* [58]. The comparison of these results is shown in Fig. 17 of Appendix B. Even in bilayer flows, the similar trend of reducing velocity and temperature upon increasing Ha is observed in the present study as shown in Fig. 10.

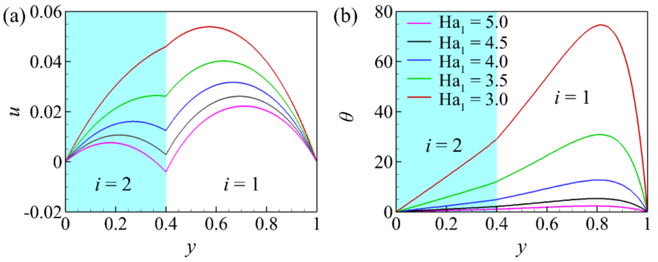

FIG. 10. Plots (a) and (b) show the variation of velocity u and temperature θ distribution across the width y of the channel for different Hartmann numbers Ha_1, respectively. The other parameters are $a = 0.4$, $\eta = 2.0$, $k = 1.5$, $\sigma = 1.0$, $Br_1 = 5.0$, and $F_1 = 2.0$.

Another important thing to note is that, for $Ha_1 = 5.0$, the velocity of the fluids at the interface becomes $u_i \leqslant 0$, and this signifies that for $Ha_1 > 5.0$ the velocity of the fluids near the interfacial region can theoretically become negative. The negative velocity of the fluids near the interfacial region for $Ha_1 > 5.0$ signifies that the fluids in that region may back-flow inside the channel upon further increase in Ha_1. This back-flow near the fluid-fluid interface may induce circulatory motion of the fluids near the interfacial region. With the increase in Ha_1, the temperature of the fluids inside the channel decreases as shown in Fig. 10(b). The temperature of the fluids declines because of the increase in radiative heat transfer due to the slow-moving fluids inside the channel as a result of increased Ha_1.

Figure 11(a) shows that, in general, Be increases across the width of the channel with the increase in Ha_1. For fluid 2, an increase in Ha_1 from 3 to 5 increases Be_2 up to 1, which signifies that the contribution of HTI to the total entropy generation in fluid 2 is essentially 100%. Although an increase in Ha_1 from 3 to 5 increases Be_1 too, the minima in Fig. 11(a) near $y = 0.8$ shows that the entropy generation due to HTI (or Be_1) at that location is negligible for fluid 1. This is because the temperature and the velocity of fluids inside the channel is maximum at this same location as shown in Fig. 10.

Figure 11(b) shows that magnetic field irreversibility parameter I_2 in fluid 2 decreases and reaches almost zero with the increase in Ha_1. Across the width of the channel ($0 \leqslant y \leqslant a$), I_2 initially decreases, goes through a minimum near $y = 0.2$, and then eventually increases near the fluid-fluid interface near $y = a$. However, the magnitude of I_2 is so insignificant ($\leqslant$0.02) in fluid 2 that its contribution to entropy generation can be ignored. In the case of fluid 1, I_1 also decreases with the increase in Ha_1; however, for a particular Ha_1 and across the width of the channel ($a \leqslant y \leqslant 1$) it initially increases, goes through a maxima near $y = 0.8$, and then eventually decreases near the channel wall.

Interestingly, the peak of I_1 in Fig. 11(b) shows that the contribution to the entropy generation due to MFI near $y =$

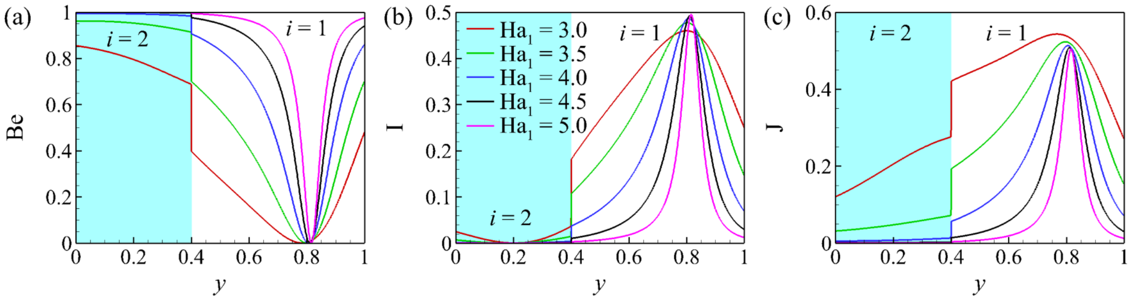

FIG. 11. Plots (a), (b), and (c) show the variation of Bejan number Be, magnetic field irreversibility parameter I, and fluid flow irreversibility parameter J across the width y of the channel for different Hartmann numbers Ha_1, respectively. The other parameters are $a = 0.4$, $\eta = 2.0$, $k = 1.5$, $\sigma = 1.0$, $\mathrm{Br}_1 = 5.0$, and $F_1 = 2.0$.

0.8 can be as high as ∼50%, whereas Fig. 11(a) shows that the contribution to the entropy generation due to HTI near $y = 0.8$ can be as low as ∼0%. This is because an increase in Ha_1 increases the effect of the Lorentz force inside the channel, which acts as a resistance to the flow. The increase in radiative heat transfer due to the slow-moving fluids inside the channel as a result of increased Ha_1 ensures that the HTI plays a significantly major role in entropy generation inside the channel for the most part. The highest temperature of fluids near $y = 0.8$ guarantees that, at that location, the entropy generation is dictated by the other two irreversibilities (MFI and FFI).

Figure 11(c) shows that J decreases across the width of the channel with the increase in Ha_1, as the velocity of the fluids inside the channel decreases due to the hinderance from the increased Lorentz force. With the increase in Ha_1 from 3 to 5, average $\mathrm{J}_2(\mathrm{J}_2^{avg})$ decreases from ∼0.2 to zero. Interestingly, the peak of $\mathrm{J}_1(\mathrm{J}_1^{\max})$ in Fig. 11(c) shows that the contribution to the entropy generation due to FFI near $y = 0.8$ can be as high as ∼50%.

Moreover, Fig. 11 shows that change in Ha_1 significantly alters the magnitude of the entropy generation inside the channel as well as the mechanism of entropy generation for both the fluids. The majority of entropy generation inside the region of fluid 2 is dictated by the HTI (∼80%–100%) with the increase in Ha_1. However, the contribution to the total entropy generation due to the three irreversibilities is shared for fluid 1 for the most part, except near the upper wall ($y = 0.8$), where entropy generation due to HTI is negligible. At this location, the entropy generation is almost equally shared by both MFI (contribution ∼ 50%) and FFI (contribution ∼ 50%).

F. Effect of Brinkman number Br_1

Figure 12 illustrates the temperature profile across the width y of the channel for increasing Brinkman numbers Br_1. Brinkman numbers (Br_i, $i = 1, 2$) signify the ratio between heat produced by viscous dissipation and heat transported by molecular conduction. With the increase in Br_1, the heat produced inside the channel by viscous dissipation increases compared to the heat transferred due to conduction, which facilitates the increase in temperature or both fluids inside the channel as shown in Fig. 12.

Figure 13(a) shows that, with the increase in Br_1, the contribution in the entropy generation due to HTI or Be increases across the channel width y. Since an increase in Br_1 increases the temperature distribution inside the channel, the entropy generation due to HTI in fluid 2 significantly increases as shown in Fig. 13(a). Although the value of Be for fluid 1 (Be_1) always remains lower ($0 \leqslant \mathrm{Be}_1 \leqslant 0.4$) than that of the fluid 2 ($0.4 \leqslant \mathrm{Be}_2 \leqslant 0.85$), but there is a visible contrast between the variation of Be_1 and Be_2. Across the channel width ($0 \leqslant y \leqslant a$), Be_2 always decreases with the increase in y, whereas Be_1 across the channel width ($a \leqslant y \leqslant 1$) initially decreases, goes through a minima $y = 0.8$, then eventually increases near the channel upper wall with the increase in y. It can be interpreted from Fig. 13(a) that, other than the global minima near $y = 0.8$, Be_1 always increase with the increase in Br_1. However, the minima in Fig. 13(a) near $y = 0.8$ shows that the entropy generation due to HTI (or Be) at that location is almost negligible. It is interesting to note that this is the same location where the temperature inside the channel is maximum as shown in Fig. 12.

Figure 13(b) shows that, for a particular Br_1, the entropy generation due to MFI (or I) initially decreases, goes through a minimum near $y = 0.2$, then increases, and goes through a maximum near $y = 0.8$. It is also interesting to note that I is always less than 0.5 throughout the channel width for all Br_1, which signifies that Be+J > I or HTI+FFI > MFI. This also represents that varying Br_1 essentially changes the

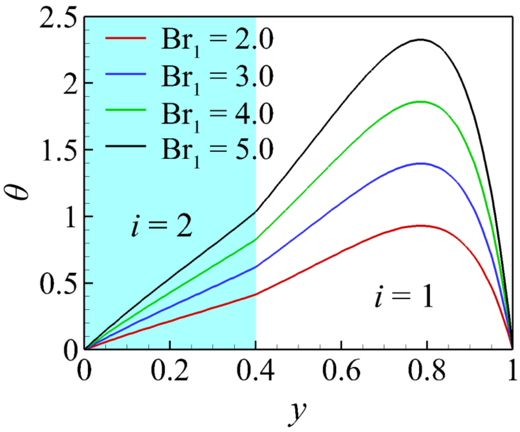

FIG. 12. The temperature θ distribution across the width y of the channel for different Brinkman numbers Br_1, respectively. The other parameters are $a = 0.4$, $\eta = 2.0$, $k = 1.5$, $\sigma = 1.0$, $\mathrm{Ha}_1 = 5.0$, and $F_1 = 2.0$.

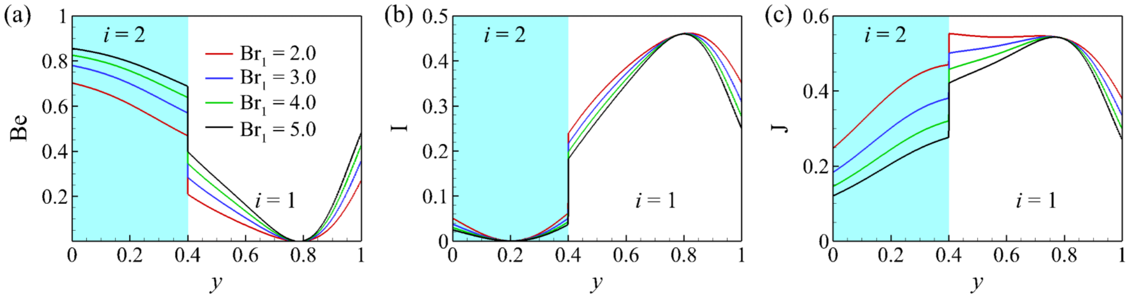

FIG. 13. Plots (a), (b), and (c) show the variation of Bejan number Be, magnetic field irreversibility parameter I, and fluid flow irreversibility parameter J across the width y of the channel for different Brinkman numbers Br_1, respectively. The other parameters are $a = 0.4$, $\eta = 2.0$, $k = 1.5$, $\sigma = 1.0$, $\mathrm{Ha}_1 = 5.0$, and $F_1 = 2.0$.

temperature profile inside the fluids, which in turn dictates the HTI and the FFI. However, the entropy generation due to the magnetic field (MFI) is not directly dependent on Br_1; rather it depends mainly on the flow and temperature profile change inside the channel due to the change in Br_1. Also, the entropy generation due to MFI (or I) near the fluid-fluid interface suddenly increases greater than ~15% from fluid 2 ($\mathrm{I}_2 < 0.05$) to fluid 1 ($\mathrm{I}_1 > 0.2$) irrespective of the value of Br_1, which is also an important factor to consider in Fig. 13(b). Figure 13(b) also shows that, other than the global minima (maxima) near $y = 0.2$ (0.8), both I_1 and I_2 always decrease with the increase in Br_1, as shown clearly in Fig. 13(b).

Figure 13(c) depicts that both J_1 and J_2 always decrease with the increase in Br_1 across the channel width. It can be seen from Fig. 13(c) that, when Br_1 is lower (2, for example), the maximum contribution to entropy generation inside fluid 2 is due to HTI (contribution ~ 70%) compared to FFI (contribution ~ 25%) and MFI (contribution ~ 5%). This is because the lesser value of Br_1 enhances the molecular conduction inside the channel, which in turn increases the entropy generation due to HTI. Figure 13(c) also shows that irrespective of the fluids the contribution to the total entropy generation inside the channel due to FFI is always within 15%–60%. This signifies that, even though Br_1 does not necessarily change the fluid flow inside the channel as such, a significant portion of the total entropy generation which is due to the FFI can be controlled by monitoring Br_1.

In summary, Fig. 13 shows that, due to the change in Br_1, the entropy generation inside the channel can be tuned by altering the mechanism of entropy generation for both fluids. The entropy generation due to HTI plays a major role for fluid 2 (contribution $\geqslant$50%), but in the case of fluid 1, the overall entropy generation is dictated by all the three irreversibilities (HTI ~ 0%–40%, MFI ~ 20%–45%, and FFI ~ 35%–55%).

G. Effect of radiation parameter F_1

Figure 14 illustrates the temperature profile across the width y of the channel for increasing radiation parameters F_1. Radiation parameters (F_i, $i = 1, 2$) signify the ratio between the radiative and conductive heat transfer. With the increase in F_1, the heat depletion from the fluids inside the channel by radiation increases compared to the heat transferred due to conduction, which facilitates the sharp decrease in temperature for both fluids inside the channel as shown in Fig. 14.

Figure 15(a) shows that, in general, Be_2 decreases with the increase in F_1. Moreover, across the width ($0 \leqslant y \leqslant a$) of the channel, it also decreases for a particular F_1. At the interface of the two fluids the magnitude of Be plummets significantly (around ~10%–30%) for a particular F_1. For fluid 1, the figure shows that, for a particular F_1, Be_1 decreases initially with the increase in y, goes through a minimum near $y = 0.8$, and then increases near the upper wall. However, it can be interpreted from Fig. 15(a) that, other than the global minima near $y = 0.8$, Be_1 always decreases with the increase in F_1. An increase in radiation parameter F_1 signifies the increase in the ratio between the radiative and conductive heat transfer, which facilitates significant temperature drops in both fluids thus ensuring the decrease in entropy generation due to the HTI (or Be).

Figure 15(b) shows that, for a particular F_1, magnetic field irreversibility parameter I initially decreases, goes through a minimum near $y = 0.2$, then increases, and goes through a maximum near $y = 0.8$. The presence of the fluid-fluid interface increases the magnitude of I by a considerably large amount (around ~ 10%–30%). It is also interesting to note that I is always less than 0.5 throughout the channel width for all F_1, which signifies that Be+J > I, or HTI+FFI > MFI. This also represents that varying F_1 essentially changes the

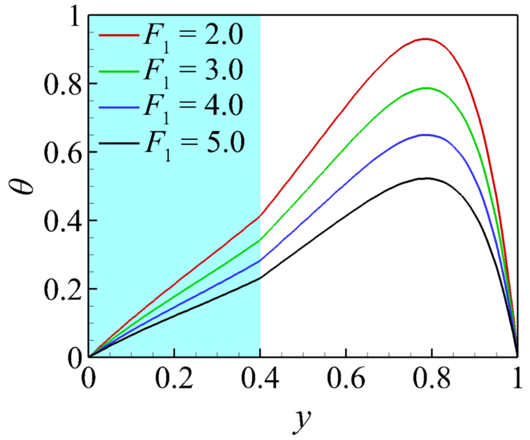

FIG. 14. The temperature θ distribution across the width y of the channel for different radiation parameters F_1, respectively. The other parameters are $a = 0.4$, $\eta = 2.0$, $k = 1.5$, $\sigma = 1.0$, $\mathrm{Ha}_1 = 3.0$, and $\mathrm{Br}_1 = 2.0$.

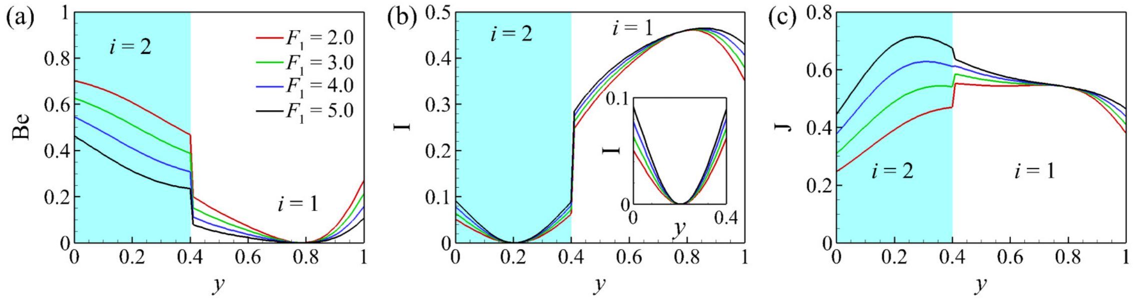

FIG. 15. Plots (a), (b), and (c) show the variation of Bejan number Be, magnetic field irreversibility parameter I, and fluid flow irreversibility parameter J across the width y of the channel for different radiation parameters F_1, respectively. The other parameters are $a = 0.4$, $\eta = 2.0$, $k = 1.5$, $\sigma = 1.0$, $\mathrm{Ha}_1 = 3.0$, and $\mathrm{Br}_1 = 2.0$.

temperature profile inside the fluids, which in turn dictates the HTI and the FFI. However, Fig. 15(b) confirms that the entropy generation due to the magnetic field (MFI) is indirectly dependent on F_1. Figure 15(b) also shows that, other than the global minima (maxima) near $y = 0.2$ (0.8), both I_1 and I_2 always increase with the increase in F_1, as shown clearly in the inset of Fig. 15(b).

Figure 15(c) illustrates that both J_1 and J_2 always increase with the increase in F_1, across the channel width. It can be seen from Fig. 15(c) that, when F_1 is higher (for example, $F_1 = 5.0$), the maximum contribution to entropy generation inside fluid 2 is due to FFI (contribution $\sim 60\%$) compared to HTI (contribution $\sim 35\%$) and MFI (contribution $\sim 5\%$). This is because the lesser value of F_1 reduces the temperatures of the fluids inside the channel, which in turn decreases the entropy generation due to HTI, so that the significant portion of the entropy generation is due to the fluid flow. However, for fluid 1, Fig. 15(c) shows that the changes in the magnitude of J_1 due to the variation of F_1 are negligible across the width of the channel ($a \leqslant y \leqslant 1$). Figure 15(c) also shows that irrespective of the fluids the contribution to the total entropy generation inside the channel due to FFI is always within 20%–70%. This signifies that even though F_1 does not necessarily change the fluid flow inside the channel as such, a significant portion of the total entropy generation which is due to the FFI can be controlled by tuning F_1.

In summary, Fig. 15 shows that, due to the change in F_1, the entropy generation inside the channel can be tuned by changing the mechanism of entropy generation for both fluids. The entropy generation due to HTI and FFI both contribute equally in the total entropy generation for fluid 2 (contribution $\sim$ 40% each); however, in the case of fluid 1, the overall entropy generation is dictated mainly by MFI ($\sim$ 30%–50%), and FFI ($\sim$ 50%–60%).

We have also asymptotically truncated the radiative flux part from the governing equations of the present mathematical formulation to match the results of Haddad *et al.* [55]. For a very low Knudsen number (Kn), the results from the present truncated formulation show a close match with the results of Haddad *et al.* [55]. The comparative plots of spatial variation of (a) velocity u, temperature θ, and (b) local Be profile are shown in Fig. 18 of Appendix B.

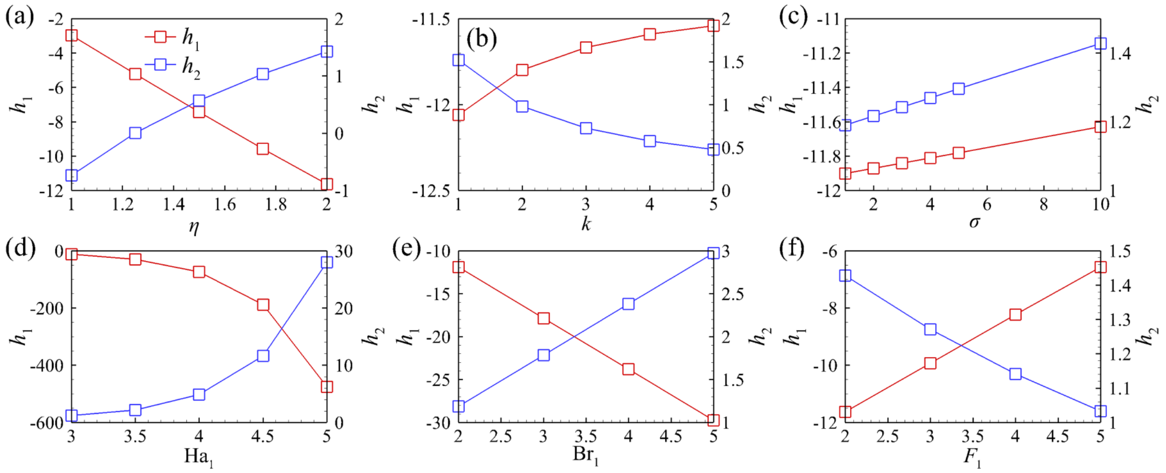

FIG. 16. Plots (a)–(f) show the variation of heat transfers, h_1 (red symbols, left side of y-axis) and h_2 (blue symbols, right side of y-axis) at the wall plates $y = 1$ and $y = 0$ for different viscosity ratios η, thermal conductivity ratios k, and electrical conductivity ratios σ, Hartmann numbers Ha_1, Brinkman numbers Br_1, and radiation parameters F_1, respectively. The other parameters are $a = 0.4$ for (a)–(f), $\eta = 2.0$ for (b)–(f), $k = 1.5$ for (a) and (c)–(f), $\sigma = 10.0$ for (a) and (f), $\sigma = 1.0$ for (b), (d), and (e), $\mathrm{Ha}_1 = 3.0$ for (a)–(c) and (e)–(f), $\mathrm{Br}_1 = 2.0$ for (a)–(d) and (f), and $F_1 = 2.0$ for (a)–(e).

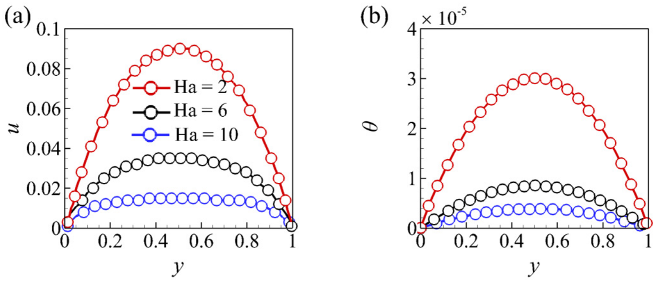

FIG. 17. Comparison of present study (circular symbols: red, black, and blue) and the analytical results (continuous lines: red, black, and blue) of Duwairi *et al.* [58]. Plots show the spatial variation of (a) velocity u and (b) temperature θ profile for increasing Hartmann numbers Ha.

H. Rate of heat transfer

The rate of heat transfer (h_1 and h_2) per unit area at the plates $y = 1$ and $y = 0$ can be obtained from,$h_1 = \frac{d\theta_1}{dy}|_{y=1}$ and $h_2 = \frac{d\theta_2}{dy}|_{y=0}$, whereas θ_1 and θ_2 can be evaluated using expressions (28) and (29). Figures 16(a)–16(f) show the variation of dimensionless heat transfers, h_1 (red symbols, left side of y-axis) and h_2 (blue symbols, right side of y-axis) at the wall plates $y = 1$ and $y = 0$ for different viscosity ratio η, thermal conductivity ratio k, electrical conductivity ratio σ, Hartmann number Ha_1, Brinkman number Br_1, and radiation parameter F_1, respectively. Figures 16(a), 16(d) and 16(e) show that the dimensionless heat transfer h_1 (h_2) decreases (increases) with the increase in η, Ha_1, and Br_1, respectively, whereas Figs. 16(b) and 16(f) show that the dimensionless heat transfer h_1 (h_2) increases (decreases) with the increase in k and F_1, respectively. However, Fig. 16(c) shows that, with the increase in σ, both dimensional heat transfer rates (h_1 and h_2) increase. The dimensionless heat transfer rates, h_1 and h_2, essentially depend on the slope of the temperature profile of the fluids near the lower ($y = 0$) and the upper ($y = 1$) walls.

Figure 16 shows that the fluid properties, like viscosity and thermal and electrical conductivity, as well as Hartmann number (magnetic field intensity), Brinkman number (temperature gradient between the fluids and the channel wall), and radiation parameters can effectively control the rate of heat transfer from the fluids to the channel walls.

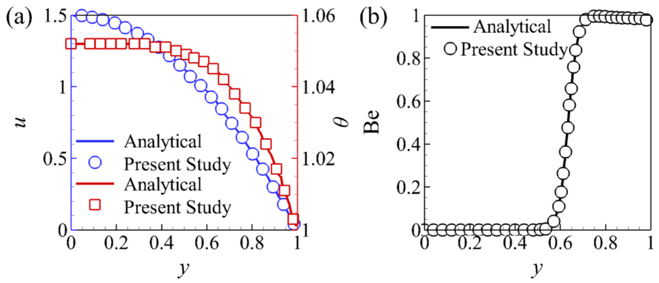

FIG. 18. Comparison of present study (discontinuous symbols: red, blue, and black) and the analytical (continuous lines: red, blue, and black) results of Haddad *et al.* [55]. Plots show the spatial variation of (a) velocity (u, blue circular symbols and continuous line, left y-axis) and temperature (θ, red square symbols and continuous line, right y-axis) and (b) distribution of the local Bejan number (Be: black circular symbol and continuous line) profile for $\mathrm{Kn} = 0.001$.

IV. CONCLUSIONS

In summary, we identify that the radiative heat transfer and transversely applied magnetic field can significantly alter the fluid flow and the heat transfer characteristics in a two-phase nonisothermal fluid flow between two infinite horizontal parallel plates under the influence of a constant pressure gradient. The velocity profile and the temperature distribution of both fluids can be tweaked with precision by altering the external magnetic field intensity as well as the temperature gradient between the fluids and the channel wall. Application of the transversely applied magnetic field is found to reduce the throughput and the temperature distribution of the fluids in a pressure-driven flow. Furthermore, the study also shows that, apart from the external handles, the inherent fluid properties, such as viscosity and thermal and electrical conductivities, can alter the velocity and temperature distribution significantly. In addition, the study confirms that the filling ratio of both fluids can vary the velocity and temperature distribution inside the channel. The rate of heat transfer at the channel walls can also be tweaked by the magnetic field intensity, temperature gradient, and fluid properties.

The study also shed light on the minute details of the entropy production due to the presence of a fluid-fluid interface. The present research addresses some of the key aspects, such as the presence of two different fluids, fluid property ratios, channel filling ratio, and relative strength of the external fields altering the flow, heat transfer, and magnetic field irreversibility within a microchannel flow. Evaluation of the entropy generation due to the heat transfer, magnetic field, and fluid flow irreversibilities reveals that the total entropy generation can be reduced to a minimum amount by efficiently controlling the Hartmann number, radiation parameter, Brinkmann number, filling ratio, and fluid properties. The discontinuity in the analysis of heat transfer, magnetic field, and fluid flow irreversibilities across the interface either enhances or reduces the amount of unretractable work associated with the system. The study also predicts the amount of the entropy production due to the three different irreversibilities and their relative contribution to the total entropy generation. This information can be a key factor in designing such flow systems because the study sheds light on the optimal design parameters needed to be maintained in order to minimize or at least reduce the overall entropy production.

The results described here can be utilized as a preliminary blueprint for developing more sophisticated MEMS devices for applications involving thermal transport. Furthermore, the present model itself can be implemented for analyzing a wide spectrum of existing EMHD transport processes across different length scales by judiciously tuning the involved nondimensional key parameters. The entropy generation, fluid flow, and heat transfer characteristics of such a confined flow can be particularly useful in the design and fabrication of a microfluidic device, which can be integrated to any state-of-the art micro-emulsifiers, mixers, reactors, flow cytometers, bioanalysis tools, and drug delivery devices for improved efficiency of existing technology.

ACKNOWLEDGMENT

The author acknowledges the support from the Department of Chemical Engineering and Centre for Nanotechnology, IIT Guwahati. The author declares no conflict of interest.

APPENDIX A: MATHEMATICAL EXPRESSIONS

The expressions for the coefficients P and Q in Eqs. (28) and (29) are given by

$$P = \frac{p_1(B_1 + B_2 a_1) + p_2 p_3}{c_1 F_1}, \tag{A1}$$

$$Q = \frac{q_1 + q_2 + q_3 + q_4 - q_5(B_3 + B_4 b_7)}{\eta M^2 d_1 F_2}, \tag{A2}$$

where p_j $(j = 1-3)$, q_m $(m = 1-5)$, a_n $(n = 1-7)$, b_l $(l = 1-12)$, c_r $(r = 1-8)$, and d_s $(s = 1-11)$ can be expressed by the following expressions:

$$\left.\begin{aligned} &p_1 = c_1 F_1(a_2 + a_3),\\ &p_2 = \mathrm{Br}_1 a_1, \quad \text{and}\\ &p_3 = c_2 + c_3 a_4 + c_4 a_5 + c_5 a_6 - c_1 c_6 a_7, \end{aligned}\right\} \tag{A3}$$

$$\left.\begin{aligned} &q_1 = -\eta M^4 d_2(b_1 + b_2) + \eta M^2 d_3 d_6(b_3 + b_4),\\ &q_2 = b_5 d_1 d_{11}(b_9 + b_{10}),\\ &q_3 = -\eta M^4 d_4(b_{10} + b_{11})(d_5 + d_6 b_{12}),\\ &q_4 = b_5^2 d_7 d_8, \quad \text{and}\\ &q_5 = b_5 b_6 d_7 d_9, \end{aligned}\right\} \tag{A4}$$

$$\left.\begin{aligned} &a_1 = \cosh(2y\sqrt{F_1}) + \sinh(2y\sqrt{F_1}),\\ &a_2 = \cosh[(\sqrt{F_1} + 2\mathrm{Ha}_1)y],\\ &a_3 = \sinh[(\sqrt{F_1} + 2\mathrm{Ha}_1)y],\\ &a_4 = \cosh(3\mathrm{Ha}_1 y) + \sinh(3\mathrm{Ha}_1 y),\\ &a_5 = \cosh(\mathrm{Ha}_1 y) + \sinh(\mathrm{Ha}_1 y),\\ &a_6 = \cosh(4\mathrm{Ha}_1 y) + \sinh(4\mathrm{Ha}_1 y),\\ &a_7 = \cosh(2\mathrm{Ha}_1 y) + \sinh(2\mathrm{Ha}_1 y), \end{aligned}\right\} \tag{A5}$$

$$\left.\begin{aligned} &b_1 = \cosh[(2\sqrt{F_2} + 4M)y\},\\ &b_2 = \sinh[(2\sqrt{F_2} + 4M)y],\\ &b_3 = \cosh[(2\sqrt{F_2} + M)y],\\ &b_4 = \sinh[(2\sqrt{F_2} + M)y],\\ &b_5 = \cosh(y\sqrt{F_2}) + \sinh(y\sqrt{F_2}),\\ &b_6 = \cosh(2My) + \sinh(2My),\\ &b_7 = \cosh(2y\sqrt{F_2}) + \sinh(2y\sqrt{F_2}),\\ &b_8 = \cosh[(\sqrt{F_2} + 2M)y],\\ &b_9 = \sinh[(\sqrt{F_2} + 2M)y],\\ &b_{10} = \cosh[(2\sqrt{F_2} + 2M)y],\\ &b_{11} = \sinh[(2\sqrt{F_2} + 2M)y], \quad \text{and}\\ &b_{12} = \cosh(2My) + \sinh(2My), \end{aligned}\right\} \tag{A6}$$

$$\left.\begin{aligned} &c_1 = F_1^2 - 5F_1\mathrm{Ha}_1 + 4\mathrm{Ha}_1^4, c_2 = A_2^2 F_1 \mathrm{Ha}_1^2 c_7,\\ &c_3 = A_1 F_1 \mathrm{Ha}_1^2 c_8, c_4 = A_2 F_1 \mathrm{Ha}_1^2 c_8,\\ &c_5 = A_1^2 F_1 \mathrm{Ha}_1^2 c_7, c_6 = 2A_1 A_2 \mathrm{Ha}_1^2 - 1,\\ &c_7 = F_1 - \mathrm{Ha}_1^2, \quad \text{and} \quad c_8 = F_1 - 4\mathrm{Ha}_1^2, \end{aligned}\right\} \tag{A7}$$

$$\left.\begin{aligned} &d_1 = 4M^4 - 5F_2 M^2 + F_2^2, d_2 = A_3^2 F_2 \mathrm{Br}_2 d_{10},\\ &d_3 = -A_4 \mathrm{Br}_2 d_9, d_4 = A_3 \mathrm{Br}_2 d_9,\\ &d_5 = 2A_4 M^2 d_{10}, d_6 = F_2 \mathrm{Ha}_2^2,\\ &d_7 = -\eta M^2 F_2 d_{10}, d_8 = M^2 A_4^2 \mathrm{Br}_2,\\ &d_9 = 4M^2 - F_2, d_{10} = M^2 - F_2, \quad \text{and}\\ &d_{11} = \mathrm{Br}_2 \mathrm{Ha}_2^2. \end{aligned}\right\} \tag{A8}$$

The coefficients $B_1, B_2, B_3,$ and B_4 in expressions (A1) and (A2) are quite cumbersome and evaluated employing the boundary conditions in the Mathematica code.

APPENDIX B: VALIDATION

We have modified the governing equations mentioned in the Secs. II B and II C to asymptotically match the governing equations of Duwairi *et al.* [58]. For this, we have taken the properties of both fluids to be the same in the present framework so that it can be assumed that a single fluid is flowing through the microchannel, which is the case for the case study of Duwairi *et al.* [58]. Figure 17 shows the effect of Hartmann number (Ha) on the dimensionless (a) velocity u and (b) temperature θ profiles, respectively, from the present study (discrete circular symbols: red, black, and blue) and the analytical (continuous lines: red, black, and blue) counterpart mentioned in Duwairi *et al.* [58]. Figure 17 shows that with the increase in Ha, the velocity u and temperature θ of the fluid decrease, which means that the electrical conductivity dictates the velocity and the temperature profiles. These findings are similar to the present study, wherein Fig. 10 shows that with the increase in Ha both the velocity and the temperature distribution decrease significantly for a bilayer flow.

The set of governing equations have also been modified to match the system considered in the study of Haddad *et al.* [55]. Employing the same approach of the present study to nondimensionalize the governing equations, we arrive at a similar conclusion with the previous results from an analytical approach [55]. Figure 18 shows the spatial distribution of (a) velocity u, temperature θ, and (b) local Bejan number Be profile for a very low Knudsen number ($\mathrm{Kn} = 0.001$). The very low value of the Knudsen number confirms that the length scale of the mean-free path of the molecules is significantly less compared to the physical length scale of the system, so essentially the fluid flow is in the continuum domain. The analytical results from the present study in Figs. 18(a) and 18(b) show a close match with the analytical results of the previous study [55]. In short, Figs. 17 and 18 asymptotically validate the results from the present formulation with the results from the previous theoretical and numerical studies.

[1] M. A. Burns, B. N. Johnson, S. N. Brahmasandra, K. Handique, J. R. Webster, M. Krishnan, T. S. Sammarco, P. M. Man, D. Jones, D. Heldsinger *et al.*, Science **282**, 484 (1998).

[2] H. Tsuchiya, M. Okochi, N. Nagao, M. Shikida, and H. Honda, Sens. Actuators B Chem. **130**, 583 (2008).

[3] L. Capretto, D. Carugo, S. Mazzitelli, C. Nastruzzi, and X. Zhang, Adv. Drug Delivery Rev. **65**, 1496 (2013).

[4] K.-i. Ohno, K. Tachikawa, and A. Manz, Electrophoresis **29**, 4443 (2008).

[5] J. S. Marcus, W. F. Anderson, and S. R. Quake, Anal. Chem. **78**, 956 (2006).

[6] H. Zhang, G. Jenkins, Y. Zou, Z. Zhu, and C. J. Yang, Anal. Chem. **84**, 3599 (2012).

[7] D. J. Eastburn, A. Sciambi, and A. R. Abate, Anal. Chem. **85**, 8016 (2013).

[8] D. R. Gossett, W. M. Weaver, A. J. Mach, S. C. Hur, H. T. K. Tse, W. Lee, H. Amini, and D. Di Carlo, Anal. Bioanal. Chem. **397**, 3249 (2010).

[9] L. Mazutis, J. Gilbert, W. L. Ung, D. A. Weitz, A. D. Griffiths, and J. A. Heyman, Nat. Protocol. **8**, 870 (2013).

[10] K. F. Jensen, Chem. Eng. Sci. **56**, 293 (2001).

[11] X. Niu, M. Zhang, J. Wu, W. Wen, and P. Sheng, Soft Matter **5**, 576 (2009).

[12] J. D. Tice, H. Song, A. D. Lyon, and R. F. Ismagilov, Langmuir **19**, 9127 (2003).

[13] A. G. Marin, W. van Hoeve, P. García-Sánchez, L. Shui, Y. Xie, M. A. Fontelos, J. C. Eijkel, A. van den Berg, and D. Lohse, Lab Chip **13**, 4503 (2013).

[14] M. Bhattacharjee, V. Pasumarthi, J. Chaudhuri, A. K. Singh, H. Nemade, and D. Bandyopadhyay, Nanoscale **8**, 6118 (2016).

[15] V. Taly, D. Pekin, A. El Abed, and P. Laurent-Puig, Trends Mol. Med. **18**, 405 (2012).

[16] A. Manz, N. Graber, and H. M. Widmer, Sens. Actuators B Chem. **1**, 244 (1990).

[17] A. T. Woolley and R. A. Mathies, Proc. Natl. Acad. Sci. USA **91**, 11348 (1994).

[18] D. Bennet and S. Kim, J. Mater. Sci. **46**, 4723 (2011).

[19] N. Convery and N. Gadegaard, Micro Nano Eng. **2**, 76 (2019).

[20] S. D. Hudson, Rheol. Acta **49**, 237 (2010).

[21] H. Wang and Y. Wang, J. Micromech. Microeng. **17**, 586 (2007).

[22] H. Foroughi and M. Kawaji, Int. J. Multiphase Flow **37**, 1147 (2011).

[23] S. Timung, V. Tiwari, A. K. Singh, T. K. Mandal, and D. Bandyopadhyay, Can. J. Chem. Eng. **93**, 1736 (2015).

[24] T. Ward, M. Faivre, M. Abkarian, and H. A. Stone, Electrophoresis **26**, 3716 (2005).

[25] T. Cubaud, Phys. Rev. E **80**, 026307 (2009).

[26] M. P. Boruah, A. Sarker, P. R. Randive, S. Pati, and S. Chakraborty, Phys. Fluids **30**, 122106 (2018).

[27] W. Ristenpart, J. Bird, A. Belmonte, F. Dollar, and H. A. Stone, Nature (London) **461**, 377 (2009).

[28] J. Chaudhuri, S. Timung, C. B. Dandamudi, T. K. Mandal, and D. Bandyopadhyay, Electrophoresis **38**, 278 (2017).

[29] S. H. Tan, B. Semin, and J.-C. Baret, Lab Chip **14**, 1099 (2014).

[30] J. Chaudhuri, T. K. Mandal, and D. Bandyopadhyay, Phys. Fluids **31**, 052005 (2019).

[31] L. Liggieri, A. Sanfeld, and A. Steinchen, Physica A **206**, 299 (1994).

[32] M. C. Weston, M. D. Gerner, and I. Fritsch, Anal. Chem. **82**, 3411 (2010).

[33] J. Chaudhuri, T. K. Mandal, and D. Bandyopadhyay, Phys. Rev. Appl. **10**, 034057 (2018).

[34] H. Chraibi, D. Lasseux, E. Arquis, R. Wunenburger, and J.-P. Delville, Phys. Rev. E **77**, 066706 (2008).

[35] J.-P. Delville, M. R. de Saint Vincent, R. D. Schroll, H. Chrabi, B. Issenmann, R. Wunenburger, D. Lasseux, W. W. Zhang, and E. Brasselet, J. Optic. Pure Appl. Optic. **11**, 034015 (2009).

[36] J. Chaudhuri and D. Bandyopadhyay, J. Colloid Interface Sci. **587**, 864 (2021).

[37] J. Meacham, M. Varady, F. Degertekin, and A. Fedorov, Phys. Fluids **17**, 100605 (2005).

[38] J. Friend and L. Y. Yeo, Rev. Mod. Phys. **83**, 647 (2011).

[39] A. Sharma, J. Chaudhuri, V. Kumar, S. Timung, T. K. Mandal, and D. Bandyopadhyay, RSC Adv. **5**, 29545 (2015).

[40] S. Timung, J. Chaudhuri, M. P. Borthakur, T. K. Mandal, G. Biswas, and D. Bandyopadhyay, Electrophoresis **38**, 1450 (2017).

[41] A. V. Lemoff and A. P. Lee, Sens. Actuators B Chem. **63**, 178 (2000).

[42] H. H. Bau, J. Zhu, S. Qian, and Y. Xiang, Sens. Actuators B Chem. **88**, 205 (2003).

[43] S. Qian and H. H. Bau, Mech. Res. Commun. **36**, 10 (2009).

[44] A. Gelb, J. P. Gleeson, J. West, and O. M. Roche, SIAM J. Appl. Math. **64**, 1294 (2004).

[45] A. Bejan, Energy **5**, 720 (1980).

[46] A. Bejan, *Entropy Generation Minimization: The Method of Thermodynamic Optimization of Finite-Size Systems and Finite-Time Processes* (CRC Press, Boca Raton, FL, 1995).

[47] J.-Y. San, Energy **35**, 1936 (2010).

[48] R. Revellin, S. Lips, S. Khandekar, and J. Bonjour, Energy **34**, 1113 (2009).

[49] A. Sciacovelli and V. Verda, Energy **34**, 850 (2009).

[50] H. Salas, S. Cuevas, and M. L. de Haro, J. Phys. D: Appl. Phys. **32**, 2605 (1999).

[51] G. Ibáñez, S. Cuevas, and M. L. de Haro, Energy Convers. Manage. **43**, 1757 (2002).

[52] G. Ibáñez, S. Cuevas, and M. L. de Haro, Int. Commun. Heat Mass **33**, 295 (2006).

[53] M. Saidi and A. Montazeri, Energy **32**, 1603 (2007).

[54] G. Ibáñez and S. Cuevas, Int. J. Therm. Sci. **47**, 1012 (2008).

[55] O. Haddad, M. Abuzaid, and M. Al-Nimr, Entropy **6**, 413 (2004).

[56] H. Abbassi, Energy **32**, 1932 (2007).

[57] H. Branover, P. S. Lykoudis, and A. Yakhot, *Liquid-Metal Flows and Magnetohydrodynamics* (American Institute of Aeronautics and Astronautics, Reston, 1983).

[58] H. Duwairi and M. Abdullah, Microsyst. Technol. **13**, 33 (2007).

[59] R. Chakraborty, R. Dey, and S. Chakraborty, Int. J. Heat Mass Transf. **67**, 1151 (2013).

[60] Y. Jian, Int. J. Heat Mass Transf. **89**, 193 (2015).

[61] M. Abdulhameed, D. Vieru, and R. Roslan, Comput. Math. Appl. **74**, 2503 (2017).

[62] M. Abdulhameed, D. Vieru, and R. Roslan, Physica A **484**, 233 (2017).

[63] Y. S. Daniel, Z. A. Aziz, Z. Ismail, and F. Salah, Eng. Lett. **26**, 107 (2018).

[64] P. D. S. Reddy, D. Bandyopadhyay, S. W. Joo, A. Sharma, and S. Qian, Phys. Rev. E **83**, 036313 (2011).

[65] R. Khanna and A. Sharma, J. Colloid Interface Sci. **195**, 42 (1997).

[66] A. Sharma, V. Tiwari, V. Kumar, T. K. Mandal, and D. Bandyopadhyay, Electrophoresis **35**, 2930 (2014).

[67] A. C. Cogley, W. G. Vincent, and S. E. Gilles, AIAA J. **6**, 551 (1968).

[68] C. J. Teo and B. C. Khoo, Microfluid. Nanofluid. **7**, 353 (2009).

[69] A. Bejan and J. Kestin, *Entropy Generation through Heat and Fluid Flow* (Wiley, New York, 1983).

[70] L. C. Woods, *The Thermodynamics of Fluid Systems* (Oxford University Press, Oxford, 1975).